Temporal separation of W and Sn mineralization by temperature-controlled incongruent melting of a single protolith: Evidence from the Wangxianling area, Nanling Region, South China

Panlao Zhao[1,2], Shunda Yuan[1*], Anthony E. Williams-Jones[3], Rolf L. Romer[4], Chen Yan[2], Shiwei Song[1], Jingwen Mao[1,2]

1. Chinese University of Geosciences, Beijing 100083, China

2.MLR Key Laboratory of Metallogeny and Mineral Assessment, Institute of Mineral Resources, Chinese Academy of Geological Sciences, Beijing 100037, China

3. Department of Earth and Planetary Sciences, McGill University, 3450 University Street, Montreal H3A 0E8, Canada

4. Deutsches GeoForschungsZentrum GFZ, Telegrafenberg, D-14473 Potsdam, Germany

*Corresponding author: Prof. Shunda Yuan

E-mail: shundayuan@cugb.edu.cn

Abstract

Tungsten and Sn display similar behaviour during magmatic processes and are commonly associated spatially and genetically with highly evolved granites. Nonetheless, they typically form separate deposits, even if their associated granites have the same protolith. This separation may be due to the fractionation of the metals at the magmatic-hydrothermal transition or their differential mobility during partial melting of the metasedimentary protolith. If this separation occurred at the magmatic-hydrothermal transition, the ages of the W and Sn deposits would be very similar, whereas, if it occurred during partial melting, the deposits are likely to have different ages because of the concentration of the metals in different magma batches and, in extreme cases, during different magmatic events.

New age data from the Wangxianling ore-field in the western part of the world-class Nanling W–Sn metallogenic province demonstrate that the W and Sn mineralization took place at different times. The W mineralization (219.5 ± 3.4 Ma) is related to Triassic granites (224.9–217.8 Ma), whereas the

Sn mineralization is related to granites of late Jurassic age (154.7 ± 1.1 Ma). This difference in ages rules out fractionation at the magmatic-hydrothermal transition as an explanation for the spatial separation of the W and Sn deposits, and implies that the separation was due to differences in the mobility of W and Sn during partial melting. Both suites of granite originated from the partial melting of the same metasedimentary rocks, and both are reduced and highly evolved. The W granites, however, have a lower zircon saturation temperature (~750 °C) than the Sn granites (~800 °C), which indicates that the magma forming the W granites was mainly the product of muscovite-dehydration melting, whereas that forming the Sn granites was largely the result of biotite-dehydration melting. The different melting paths indicate that W released during muscovite breakdown dissolved in the magma, whereas Sn was sequestered by restite biotite. At the higher melting temperature, the residual W and Sn, released during the subsequent breakdown of biotite, dissolved in the magma. Thus, the magma generated at low temperature was enriched in W, leading to subsequent W mineralization, whereas the magma generated at high temperature was enriched in Sn and produced a Sn-mineralized granite.

The whole–rock Sr–Nd isotopic data for the Triassic W granites plot in the compositional field of the regional basement rocks and are consistent with partial melting of an orogenically thickened crust by internal heating in a collisional setting. In contrast, the Sr-Nd isotopic data for the Late Jurassic Sn(–W) granites are displaced toward a mantle composition, likely reflecting contributions from mantle-derived material. Given the emplacement of many of the Late Jurassic Sn(–W) granites close to the Chenzhou–Linwu Fault, we propose that this structure was the focus of decompression melting of the mantle and the injection of mantle-derived melts into the crust during the Late Jurassic, which supplied the additional heat for the melting at higher temperature needed to generate magmas enriched in Sn. This model, which is based on differences in the behaviour of Sn and W during crustal melting, is potentially applicable to other Sn-W metallogenic provinces where Sn and W deposits are temporally separated.

Keywords: melting temperature; W and Sn mineralization; granite; hydrothermal deposits; Nanling Region

1 Introduction

Granite-related magmatic-hydrothermal ore deposits supply most of the World's W and Sn (Lehmann, 1990; Brown and Pitfield, 2014). Owing to their highly incompatible nature, W and Sn are usually concentrated in crustally-derived, highly fractionated, reduced granitic rocks (Ishihara, 1981; Simons et al., 2016, 2017; Gardiner et al., 2017, 2018), which occur in discontinuous belts along the margins of cratons, where sedimentary protoliths are voluminous (Romer and Kroner, 2015, 2016). Tungsten and Sn are sourced from similar protoliths and are mobilized (partial melting) and enriched (fractional crystallization) by broadly similar processes. Therefore, it is not unreasonable to predict that W and Sn should concentrate in the same deposits or ore fields, as is the case for many world-class W–Sn deposits, such as those of the Shizhuyuan (China) and Mole (Australia) districts. Nonetheless, the two metals more commonly form separate deposits (or at least deposits in which one metal predominates over the other). Possible explanations for the separation of W and Sn mineralization at the deposit or intrusion scale include: (i) the different partitioning of Sn and W into the fluid and magma at the magmatic-hydrothermal transition (Audétat et al., 2000a, 2000b; Schmidt et al., 2020) and; (ii) differences in the behaviour of W and Sn during fractional crystallization at different redox conditions (Blevin and Chappell, 1992; Blevin et al., 1996). These hypotheses, however, are not sufficient to explain the separation of W and Sn mineralization at the scale of an entire metallogenic belt with both metals being related to reduced, highly evolved granites (Yuan et al., 2019). Instead, the cause for the contrasting regional distribution of W and Sn mineralization must lie in the composition of the protoliths, the melting conditions, or both (Simons et al., 2017; Wolf et al., 2018; Yuan et al., 2019). Yuan et al. (2019) proposed that the temperature of protolith-melting was responsible for the spatial-decoupling of W and Sn mineralization in some parts of the Nanling W–Sn metallogenic province, South China. However, a difference in the W and Sn contents of the basement rocks, which are considered to be the protoliths for the deposit-related granites, is an alternative explanation for the separation of W and Sn mineralization in the Nanling province. This alternative was not considered by Yuan et al. (2019). We have therefore built on this earlier province-wide study of the distribution of W and Sn mineralization in the Nanling metallogenic province (Yuan et al., 2019) by restricting the current study to W and Sn mineralization in granites in a single basement block that likely provided a single protolith for the magmas.

The Nanling region is one of the largest W–Sn metallogenic provinces in the world, and accounts for more than 54% of global W resources and significant resources of Sn (Yuan et al., 2018). Although most of the deposits formed during the Late Jurassic (160–150 Ma, Mao et al., 2007; Yuan et al., 2011; Zhao et al., 2016, 2018), there are also many Late Triassic deposits (Fig. 1B, Hu and Zhou, 2012; Mao et al., 2011, 2019; Hu et al., 2017). The latter mainly contain W mineralization, whereas the Late Jurassic deposits are dominated by Sn but also contain significant W mineralization (Fig. 1B). Triassic W deposits and Jurassic Sn(–W) deposits occur in close proximity to each other in the western part of the Nanling region (Fig. 1B), which makes it an ideal location for investigating the temporal separation of Sn and W deposits.

The Wangxianling W–Sn polymetallic ore-field is located in the western part of the Nanling Region, and hosts a Sn reserve of 0.19 Mt Sn and a W reserve of more than 0.11 Mt WO_3 (Mao et al., 2013; Zhang et al., 2015). The tungsten deposits occur mainly in the northern and western parts of the ore field and are spatially related to the Triassic Wangxianling pluton, whereas the major Sn deposits are concentrated in the southeastern part and are spatially associated with Late Jurassic biotite granites and granite porphyries (Fig. 2A). Although field relationships in the area suggest that the W and Sn mineralization might also be of Triassic and Late Jurassic age, respectively, the ages of the deposits have not been reliably determined and thus the temporal relationships of this mineralisation to the intrusions has still to be established.

In this study, we report new zircon U–Pb ages for the Wangxianling pluton and a molybdenite Re–Os isotopic age for the spatially associated W mineralization. Using this information and a compilation of geochemical and isotopic data for the ore-related granites in the western part of the Nanling Region, we evaluate the processes that may have influenced the separation of W and Sn mineralization.

2 Regional geological setting

The South China Block is composed of the Yangtze Block to the northwest and the Cathaysia Block to the southeast, which were sutured to the Qinhang tectonic belt between 1.1–0.83 Ga (e.g., Chen and Jahn, 1998; Zhao et al., 2011). After this Neoproterozoic amalgamation, the South China Block was subjected to the Kwangsian orogeny in the middle Paleozoic, collided with the Indosinian Block (to the southwest) and the North China Craton (to the north) in the Triassic (258–243 Ma; Carter et al., 2001), and was affected by westward subduction of the Paleo-Pacific plate in the Jurassic and the Cretaceous.

The Nanling Region is located in the central part of the South China Block (Fig. 1A) where the basement is dominated by slates, phyllites, and schists representing sequences of clastic sedimentary rocks that were metamorphosed to greenschist or amphibolite facies during the mid-Paleozoic Kwangsian orogeny. The age of detrital zircon in these rocks shows that they were mainly deposited during the Neoproterozoic to Silurian and were derived from the erosion of Neo- and Meso-Proterozoic protoliths and to a minor extent from an Archaean protolith (Yu et al., 2006, 2010); their chemical composition indicates a high degree of maturity (Wei et al., 2009). This metamorphic basement was overlain by upper Devonian to lower Triassic marine sedimentary rocks consisting mainly of limestones, marls, and minor siltstones. These rocks, in turn, were unconformably overlain by upper Triassic to lower Cretaceous continental siliciclastic rocks, which are sparsely exposed in the eastern part of the Nanling Region and comprise sandstone, siltstone, conglomerate, tuff, and continental red beds (Fig. 1B). The NE-trending Chenzhou–Linwu Fault, which lies in the central part of the Qinhang belt, is one of the largest faults in the Nanling Region.

There were several episodes of widespread igneous activity in the Nanling Region that are closely related to early Paleozoic and late Mesozoic tectono-thermal events (Fig. 1B). The early Paleozoic magmatism is represented by Silurian-Devonian granitic plutons, mainly batholiths, in the central and western parts of the Nanling Region. The Triassic granites, however, typically form small plutons and batholiths that are dispersed over the entire region. These younger intrusions invariably contain large proportions of aluminous minerals, such as muscovite, garnet and tourmaline, and formed in a late-collisional event (234–205 Ma), albeit in an extensional setting (Zhou et al., 2006). The Late Jurassic (160–150 Ma) granites are the most voluminous and represent the most important magmatic event from the perspective of W-Sn mineralisation. Although these granites were mainly derived from partial melting of the crust, there are also sporadic occurrences of Jurassic mafic rocks (e.g., the Daoxian basalt with an ^{40}Ar-^{39}Ar age of ~150 Ma; Li et al., 2004) and granodiorites (zircon U-Pb ages of 160-150 Ma; Jiang et al., 2009; Yang et al., 2016; Zhao et al., 2016, 2017) along the Chenzhou–Linwu Fault zone that may partly or wholly have originated in the mantle (Fig. 1B). The Jurassic igneous rocks formed in an intra-arc rift setting that developed in response to changes in the subduction of the Paleo-Pacific plate (Jiang et al., 2009) or as a result of the breakup of this plate (Mao et al., 2013).

The extensive W and Sn mineralisation in the Nanling Region was the product of multiple pulses of igneous activity, although the most important W–Sn mineralisation, economically, accompanied the Late Triassic and particularly the Late Jurassic magmatic events (Hu et al., 2012; Mao et al., 2019). The Late Triassic magmatism produced granites that are spatially associated with W-deposits in the western part of the Nanling Region (Fig. 1B), whereas the Late Jurassic (160–150 Ma) magmatism gave rise to granites that are associated with Sn(-W) deposits in the western part of the region, especially in vicinity of the NE-trending Chenzhou-Linwu Fault (Fig. 1B). Information on the nature of the deposits, their ages and the ages of the associated granites are provided in Table 1.

3 Geology of the Wangxianling area

3.1 Stratigraphy and structure

Strata exposed in the Wangxianling area consist mainly of Devonian and Carboniferous sedimentary rocks. The lower part of the Middle Devonian sequence is composed of quartz sandstone, siltstone, and shale, with conglomerate-bearing sandstone and conglomerate beds at the base, whereas the upper part of the Middle Devonian sequence and the Upper Devonian sequence consists mainly of dolomitic limestone, micritic limestone, and chert-bearing limestone. Carboniferous sedimentary rocks overly the Devonian strata conformably, and are composed of marl, limestone, and dolomitic limestone as well as subordinate siltstone, shale, and sandstone. The structural framework consists of NNE-, NE- and E-W-striking faults. In the southeastern part of the Wangxianling area, NE-striking faults controlled the shapes of the granite porphyry and biotite granite intrusions (Fig. 2A).

3.2 Intrusive rocks

The Wangxianling pluton is the main intrusive body exposed in the Wangxianling area, and is composed of two textural facies, which are otherwise mineralogically and geochemically similar (Fig. 2A, 3). The central part of the pluton consists mainly of coarse- to medium-grained tourmaline-bearing two-mica granite (Fig. 3A, B), which is composed of quartz (~30%), K-feldspar (~40%), plagioclase (25%), muscovite (~4%), biotite (~3%), and tourmaline (1%–3%). Accessory minerals include apatite, zircon, monazite-(Ce), and rutile. The marginal facies has a similar mineral assemblage to the central facies, but is fine- to medium-grained and contains more muscovite and tourmaline (Fig. 3C, D).

The coarse-grained Hehuaping biotite granite is exposed to the southeast of the Wangxianling pluton (Fig. 2A and 4A), and is composed (Fig. 3E, F) mainly of quartz (~35%), K-feldspar (~35%), plagioclase (~20%), and biotite (~5%). Accessory minerals include apatite, zircon, monazite-(Ce), and rutile.

More than twenty granite porphyry dykes were emplaced in the Devonian carbonates in the southeastern part of the Wangxianling area (Fig. 2). These dykes are 200 m to > 1000 m long and 15 to 80 m wide. The granite porphyry contains phenocrysts (~50%) of quartz, K-feldspar, and plagioclase, and the matrix, which commonly exhibits micro-subhedral to xenomorphic granular textures, consists of quartz, K-feldspar, and plagioclase with accessory apatite, zircon, and rutile.

3.3 The ore deposits

The Wangxianling area hosts numerous W ore deposits along the northern and western margins of the Wangxianling pluton, of which the Shuiyuanshan deposit is the most important (Fig. 2A). The primary mineralisation comprises scheelite in greisen, which is accompanied by subordinate wolframite-bearing quartz veins (Fig. 2 and 5). There is also secondary residual mineralization that takes the form of scheelite-bearing unconsolidated Quaternary sediments, which formed *in situ* by weathering of the greisen orebodies (Hou et al., 2015). Drill hole records show that the scheelite ores are part of a well-defined zonation from the surface to the tourmaline two-mica granite (Fig. 2C), which comprises: (i) a 0.1–10 m thick soil layer; (ii) a 2–110 m thick gravel-bearing layer enriched in scheelite; and (iii) scheelite-bearing greisen and tourmaline-bearing two-mica granite. The gravel layer hosts abundant fragments of intensely weathered greisen and tourmaline-bearing two-mica granite of variable grain-size (2–30 cm diameter). Locally, there are also intercalated sandstone and conglomerate layers. Scheelite occurs mainly in the matrix of these layers.

There are two major orebodies exposed by the Shuiyuanshan tungsten mine, a residual orebody and a greisen-scheelite orebody. The residual scheelite orebody is stratiform, >1200 m long, > 800 m wide, and on average ~50 m thick, and lies above the roof of the Wangxianling granite. This orebody hosts a WO_3 resource of 89,400 t, with an average grade of 0.11wt.% WO_3. The greisen orebody is about 600 m long, 400 m wide and 5–80 m thick, and contains a WO_3 resource of 15,000 t (average WO_3 grade of 0.28%). The ore minerals are scheelite, molybdenite, and pyrite, and the gangue minerals are quartz, muscovite, and topaz. In addition, there are some wolframite-bearing quartz–veins in the upper part of the intrusion (Fig. 2B and 5E and 5F).

The Hehuaping Sn deposit is located in the southeastern part of the Wangxianling area and is spatially associated with biotite granite and granite porphyry dykes. There are five main orebodies, all of which are associated with NE-trending faults (Fig. 4A). In orebody III, cassiterite occurs as disseminated, vein, and veinlet mineralisation in granite porphyry dykes. This orebody is 370 m long, 3–18 m wide and has an average Sn grade of 0.51%. The other orebodies are related to magnesian skarn. Among them, orebody IV is the most important. It is a stratiform orebody located at the contact between Devonian dolomitic limestone and sandstone (Fig. 4B). In the upper part of the biotite granite pluton, there is evidence of extensive greisenisation and chloritisation and in the Devonian carbonates, there is a well-developed zonation from forsterite–spinel–diopside skarn to phlogopite–chlorite-serpentine skarn, cassiterite–magnetite–diopside skarn, and dolomitic marble (Yao et al., 2014). The tin orebody mainly developed during the cassiterite-magnetite-diopside stage as a stratiform unit at the base of the magnesian skarn. It is approximately 3400 m long, 300–600 m wide, and 5–16 m thick with a Sn reserve of 85,000 t (average grade 0.61%). Cassiterite is the main tin mineral and occurs mainly as small grains with sulfide minerals and magnetite (Fig. 5G). The sulfide minerals are sphalerite, galena, pyrite, and arsenopyrite, and the gangue minerals are quartz, muscovite, chloride, fluorite, and calcite.

4 Samples and analytical methods

Zircon used for U–Pb dating was obtained from medium-grained (SYS–9) and fine-grained (SYS–3–3–4) tourmaline-bearing two-mica granite in the Shuiyuanshan W mine (Fig. 2B) and from biotite granite (SYS–7) in the Hehuaping Sn mine (Fig. 4B). Molybdenite for Re–Os dating (sample SYS-8) was collected from the greisen-type ore of the Shuiyuanshan W mine. Zircon and molybdenite grains were separated using standard magnetic and heavy liquid techniques and were subsequently handpicked under a binocular microscope.

4.1 Zircon LA–MC–ICP–MS U–Pb dating

Representative zircon crystals were mounted in epoxy resin and then polished to expose their interiors. These crystals were examined in transmitted and reflected light as well as by cathodoluminescence (CL) to reveal their internal structures and to select the optimum laser targets.

A NewWave UP 213 laser ablation system coupled to a Finnigan Neptune MC–ICP–MS was used for the zircon U–Pb dating. This equipment is located at the Key Laboratory of Metallogeny and Mineral Assessment, Institute of Mineral Resources, Beijing, China. The laser was operated using a 30 μm spot width and a 10Hz repetition rate and the ablated material was transported to the torch of the MC–ICP–MS using He as a carrier gas. The ICPMSDataCal software was used for off-line selection and integration of the background and analytical signals, as well as time-drift correction and quantitative calibration for U–Pb dating (Liu et al., 2008). Groups of 5–10 measurements of unknown zircon crystals and crystal fragments were bracketed between three measurements of zircon standard samples GJ–1 (n = 2) and the Plesovice standard (n=1). Concordia diagrams were prepared and weighted mean calculations made using Isoplot/Ex Version 3.0 (Ludwig, 2003). Details of the analytical procedures are given by Hou et al. (2009).

4.2 Molybdenite Re–Os dating

Molybdenite Re–Os isotope data were obtained using a Thermo Electron TJA X–series ICP–MS instrument at the National Research Center of Geoanalysis, Chinese Academy of Geosciences, Beijing, China, and analytical procedures described by Du et al. (2004). The Re–Os model ages were calculated using the relationship $t = [\ln(1+{}^{187}Os/{}^{187}Re)]/\lambda$, where λ is the ^{187}Re decay constant of 1.666×10^{-11}/year (Smoliar et al., 1996). The Re–Os isochron age was calculated using the ISOPLOT 2.49 program (Ludwig, 2001). Estimates of the uncertainty in the Re–Os model ages comprise a 1.02% uncertainty in the ^{187}Re decay constant and uncertainties for spike calibration and mass spectrometry (Du et al., 2004).

5 Results

5.1 Zircon U–Pb ages

The separated zircon crystals and fragments are generally colorless, transparent, euhedral, and range in length between 70 and 220 μm with length/width ratios of 1 to 4. Most of the crystals display fine oscillatory zoning in cathodoluminescence images (Appendix Fig. A1), suggesting that they had a magmatic origin (Hoskin and Schaltegger, 2003). The results of *in situ* zircon U–Pb analyses are presented in Table 1 and illustrated in Fig. 6. Eighteen analyses were made of zircon from the coarse-grained tourmaline-bearing two-mica granite (SYS–9). The zircon crystals have highly variable U contents of 1,291-6,933 ppm and the Th/U ratios vary between 0.1 to 0.7, mostly clustering around 0.1–0.4 (Table 1). Although the U concentrations are highly variable, there is no correlation between the apparent $^{206}Pb/^{238}U$ age and the U content (Appendix Table A1), indicating that there was not a noticeable high-uranium matrix effect (White and Ireland, 2012). Sixteen analyses yielded a weighted mean age of 224.9 ± 2.3 Ma (MSWD = 0.8) (Fig. 6A), which is interpreted to be the best estimate for the crystallization age of sample SYS–9. Two analyses (SYS–9–2 and SYS–9–9) of inherited zircon cores yielded model $^{206}Pb/^{238}U$ ages of 252.6 and 250.7 Ma. Zircon crystals from the medium-grained tourmaline-bearing two-mica granite (sample SYS–3–3–4) have even more variable U contents (2706–

10792 ppm) than those from the coarse-grained tourmaline-bearing two-mica granite; the Th/U ratios mostly vary between 0.1 to 0.3 (Table 1). There also is no correlation between the U content and the apparent $^{206}Pb/^{238}U$ age. Based on 16 analyses, the best estimate of the crystallization age of sample SYS–3–3–4 is 217.8 ± 3.9 Ma (MSWD = 2.8) (Fig. 6B). Zircon crystals from the biotite granite (sample SYS–7) have moderately variable concentrations of U (368–2,216 ppm) and Th (167–1,351 ppm), with Th/U ratios ranging from 0.2 to 0.8 (Table 1). The weighted mean age of 18 analyses is 154.7 ± 1.1 Ma (MSWD = 1.1) (Fig. 6C) and is interpreted to be the age of the crystallization of sample SYS–7.

5.2 Molybdenite Re–Os ages

The results of five molybdenite Re–Os analyses are listed in Appendix Table 2 and illustrated in Fig. 6D. The total Re and ^{187}Os concentrations vary from 2,908 to 9,822 ng/g, and from 6.71 to 22.41 ng/g (Appendix Table 2), respectively. The five Re–Os model ages range from 216.2 ± 3.0 to 222.7 ± 3.0 Ma, and the weighted mean age is 219.5 ± 3.4 Ma (MSWD = 3.2). The isochron age for the five samples is 219 ± 13 Ma with a MSWD of 8.9 (Fig. 6D). Considering that the Re–Os model ages vary in a relatively narrow range, the weighted mean of 219.5 ± 3.4 Ma is interpreted as the age of molybdenite crystallization in the Shuiyuanshan W deposit.

6 Discussion

6.1 Spatially coincident but temporally separate W and Sn mineralization in the Wangxianling ore-field

The Nanling W–Sn polymetallic metallogenic province experienced multiple tectonic-magmatic events and associated mineralization (Mao et al., 2013; Yuan et al., 2015). The W-Sn mineralization in this and other W-Sn metallogenic provinces is temporally and genetically associated with highly evolved late-stage intrusions in composite plutons (Lehmann, 1990) that contain early W- or Sn-barren phases (Yuan SD et al., 2018; Yuan YB et al., 2018). Therefore, to better constrain the timing of mineralization, it is necessary to date the ore minerals directly (Yuan et al., 2011).

The Shuiyuanshan deposit hosts much of the W mineralization in the Wangxianling ore-field, of which the greisen-type ore is the most important economically. Until this study, however, there had been no direct dating of the ores. A molybdenite sample collected from the greisen yielded a Re–Os age of 219.5 ± 3.4 Ma, which is similar to the U–Pb ages of 217 ± 3.9 Ma and 224.9 ± 2.3 Ma obtained for zircon crystals collected from the tourmaline-bearing two-mica granite (Fig. 6). This indicates that the W mineralization in the Wangxianling area was temporally related to the emplacement of the Late Triassic Wangxianling pluton.

Zircon collected from the biotite granite in the Hehuaping Sn deposit yielded a U–Pb age of 154.0 ± 1.3 Ma, which is similar to the U–Pb age of 157.8–154.8 Ma obtained for cassiterite from the skarn (Zhang et al., 2015). This indicates that Sn mineralization in the Wangxianling area is temporally related to the Late Jurassic biotite granite (Fig. 2A and 3). The geochronological data, therefore, show that there were two episodes of mineralization in the Wangxianling ore-field, a Late Triassic episode of W mineralization and a Late Jurassic episode of Sn mineralization.

6.2 The contribution of temperature-controlled incongruent melting to the temporal separation of W and Sn mineralization in the Wangxianling area

There are three factors that can potentially contribute to the separation of W and Sn during their transport to the site of deposition: (1) the temperature of protolith melting (Simons et al., 2016, 2017; Yuan et al., 2019); (2) the redox state and degree of fractionation of the magma (Van Middelaar and Keith, 1990; Blevin and Chappell, 1992; Blevin et al., 1996; Baker et al., 2005); and (3) the conditions of fluid-melt separation (Audétat et al., 2000a, 2000b; Schmidt et al.,2020). Late stage processes during magma crystallisation, in particular the separation of an aqueous fluid can result in large-scale zonation of W and Sn mineralisation at the deposit scale (Audétat et al., 2000a, 2000b; Schmidt et al., 2020). This, however, does not apply in the Wangxianling area, where the W mineralization is related to a Late Triassic pluton and the Sn mineralization to a Late Jurassic pluton. Blevin and Chappell (1992) proposed that Sn mineralization is associated with reduced granites because of the high solubility of tin as Sn^{2+} and its relative insolubility as Sn^{4+}, whereas W mineralization can be associated with both oxidised and reduced granites because it dissolves exclusively as W^{6+} (Linnen et al., 1995; O'Neill et al., 2008). From Figures 7A and B, however, it is evident that the redox states of the Wangxianling and Hehuaping granites are quite similar, and that both classify as transitional between magnetite and ilmenite series granites (Ishihara, 1981). The low magnetic susceptibility of these granites, which is less than 1×10^{-4} emu/g is consistent with this conclusion (Zhang et al., 2016). In addition, there is no correlation between their Fe_2O_3/FeO and Rb/Sr ratios (Fig. 7B), implying that the redox state did not change during fractional crystallization (Sato, 2012; Richards, 2015). It is also noteworthy that the Wangxianling and Hehuaping granites have broadly overlapping chemical compositions (SiO_2 and TiO_2 contents) and Rb/Sr, and Zr/Hf ratios (Fig. 7), showing that they are highly evolved granites which experienced a similar degree of fractional crystallization. Furthermore, the Sn and W contents of the two granitic magmas increased as the degree of fractionation increased (Fig. 7C-F), showing that fractional crystallization did not result in the depletion of either Sn or W. Therefore, the observation that the W and Sn mineralization in the Wangxianling ore-field is related to separate granites cannot be explained by differences in the redox state or degree of fractionation of the corresponding magmas.

As the separation of W from Sn in the Wangxianling ore-field cannot be explained, either by differences in the conditions of fluid phase exsolution or differences in the oxidation state and degree of fractionation of the magmas, it follows that the separation must have been due to the conditions of partial melting of the source rocks. This hypothesis posits that the temperature at which the metasedimentary protolith melts determines whether Sn and W are released to the melt or remain in the restite (Simons et al., 2017; Wolf et al., 2018; Yuan et al., 2019). The basis for the hypothesis is that muscovite, which melts at relatively low temperature, is the principal host for W in the protolith (its ability to sequester W is shown by the high muscovite-melt partition coefficient for W; Appendix Table A5) and that biotite, which melts at higher temperature is an important host for Sn. It is also supported by the observation that none of the other minerals that might be present in the sedimentary protolith at the mid-crustal depths of melting (quartz, garnet, cordierite, K-feldspar, sillimanite, plagioclase, orthopyroxene and ilmenite; Appendix Fig. A3) are likely to be able to sequester significant Sn and W and be potential hosts for these metals based on their mineral-melt partition coefficients (Appendix Table A5, Simons et al., 2017). Thus, a magma produced by melting of a Sn-W-bearing metasedimentary protolith at relatively low temperature would be preferentially enriched in W, whereas a magma produced at higher temperature would be enriched in Sn. Moreover, release of magma produced at low temperature from a protolith that subsequently melted at higher temperature would deplete the latter magma in W and increase its Sn/W ratio.

In order to test the above hypothesis for the Wangxianling ore-field, we estimated the melting temperatures of the protoliths for the two granites using the zircon-saturation geothermometer (Watson and Harrison, 1983), which has been widely used to determine the initial magma temperature (e.g., Chappell et al., 1998, 2000; Miller et al., 2003; Huang er al., 2011; Yuan et al., 2019). Because zircon is an early saturating mineral, samples of the least evolved granite (Fig. 8A-B) were chosen for this purpose. These estimates show that the magma for the Wangxianling W granite was generated at a significantly lower temperature (743 ± 15 °C) than that for the Hehuaping Sn granite (806 ± 19 °C, Fig. 8A-B; Appendix Table A3). The presence of abundant inherited zircon in the Triassic Wangxianling granite (Zhang et al., 2015 and this study) indicates that the corresponding magma was saturated with respect to zircon at the onset of melting. It also indicates that the bulk Zr content of the granite overestimates the concentration of Zr dissolved in the magma and, in turn, its initial temperature (cf. Miller et al., 2003). In contrast, the rarity of inherited zircon in the Jurassic Hehuaping granite implies that the magma from which it crystallized was initially just saturated or possibly even undersaturated with respect to zircon and that its initial temperature may have been underestimated. Consequently, the difference in the initial temperatures of the magmas forming these two granites might be greater than reported above. As muscovite is the only major phase that undergoes substantial dehydration melting at temperatures < 800 °C (Viruete et al., 2000; Miller et al., 2003), this supports our hypothesis that the Wangxianling W granite was generated by muscovite-mediated melting, whereas the Hehuaping Sn granite was generated by biotite-dehydration melting at a higher temperature (806 ± 19 °C). In principle, additional support for this hypothesis can be provided by the bulk rock Pb/Ba and Al_2O_3/TiO_2 ratios of the granites, which should differ greatly depending on whether they were the products of magmas generated by dehydration melting of muscovite or biotite. This is because: 1) Pb has a strong preference for muscovite over biotite and its release to the magma is much greater during the melting of muscovite

(Finger and Schiller, 2012; Ewart and Griffin, 1994); 2) muscovite contains a much higher proportion of Al than biotite and thus the proportion of Al released to the magma is correspondingly higher during melting of muscovite; 3) the high mineral/melt coefficient for Ba (Icenhower and London, 1995) inhibits its release to the magma until high temperature and; 4) the breakdown of Ti-bearing minerals, such as ilmenite and biotite, occurs mainly at the higher temperature of biotite melting (Patiño Douce and Johnston, 1991). Thus, granites resulting from the dehydration melting of muscovite should have much higher Pb/Ba and Al_2O_3/TiO_2 ratios than those resulting from the dehydration melting of biotite. We used the least evolved samples for each pluton to evaluate these ratios, as fractional crystallization modifies Pb/Ba and Al_2O_3/TiO_2 ratios and, as expected, the W-mineralized Wangxianling granite has much higher Pb/Ba and Al_2O_3/TiO_2 ratios than the Sn-mineralized Hehuaping granite (Fig.8c and d), thereby further supporting our hypothesis that W was mainly concentrated during dehydration melting of muscovite, whereas Sn was mainly concentrated during dehydration melting of biotite.

For the reasons given above, we conclude that the association of the W mineralization with the Wangxianling granite and the Sn mineralization with the Hehuaping granite is a direct consequence of the different melting temperatures of these two granites. Moreover, as the Hehuaping mineralization is relatively depleted in W, we propose that the release of W from the protolith during Triassic melting exhausted the supply of W, leaving little or no W for the Jurassic melting event. In summary, Triassic muscovite-dehydration melting and Jurassic biotite-dehydration melting of the same metasedimentry protolith provided an effective mechanism for temporally separating W- from Sn-mineralized granites in the Wangxianling area.

6.3 Heat sources controlling W-Sn mobilization

The western part of the World-class Nanling W–Sn metallogenic province is characterized by Late Triassic W and Late Jurassic Sn(-W) mineralization (Fig. 1B). Both types of mineralisation are genetically related to highly evolved peraluminous granites that crystallized at low oxygen fugacity (Appendix Table A3). The Late Triassic W granites, however, were the products of melting at significantly lower temperature (~750 °C) than the Late Jurassic Sn(-W) granites (~800 °C; Fig. 10 and Appendix Fig. A2). Therefore, as in the Wangxianling area, the separation of the Late Triassic W and

Late Jurassic Sn(-W) mineralization in the western part of the Nanling region is interpreted to have resulted from differences in the melting temperature of the protolith that generated the corresponding granitic magmas. The difference in temperature, in turn, indicates that there were differences in the heat sources for the two magmatic events due to differences in their plate-tectonic settings.

Large volumes of peraluminous granitic rocks were generated by melting of continental crust during the Early Triassic, as a result of continent-continent collision, with little or no input of heat from the mantle or addition of mantle-derived magma (Zhou et al., 2006; Wang et al., 2007, 2013). In the absence of heat from the mantle, the maximum temperature was relatively low and consequently muscovite-dehydration melting dominated (Miller et al., 2003; Romer and Kroner, 2016). The Shuiyuanshan tourmaline-bearing two-mica granite and other Late Triassic W-mineralized granites of the Nanling region have Sr–Nd isotopic compositions similar to those of the regional basement (Fig. 8 and 9). Therefore, this basement is interpreted to have been the source of the Late Triassic granites. The amount of melt produced during muscovite-dehydration melting is determined by the amount of muscovite (Miller et al., 2003), which is greatest in Ca-poor sedimentary rocks (the presence of Ca promotes the crystallization of plagioclase at the expense of muscovite during regional metamorphism; cf. Wolf et al., 2018). Thus, the generation of pluton-scale volumes of magma by muscovite-dehydration melting requires a muscovite-enriched sedimentary protolith of high enough maturity to have lost virtually all its Ca during chemical weathering (Romer and Kroner, 2015, 2016). This is considered to have been the case for the protolith of W-mineralized granites (Romer and Kroner, 2016; Song et al., 2018; Mao et al., 2019). We therefore conclude that partial melting of the basement at low temperature (~750 °C) can explain the enrichment of W in the Triassic granites and their association with the W deposits.

The temperature (~800 °C) required to generate the magmas that produced the Sn-enriched Late Jurassic (160–150 Ma) granites and associated Sn(–W) deposits in the Nanling region was higher than for the W-enriched Triassic magmas because of the need to melt biotite, the principal host for Sn. Such a high melting temperature requires the input of heat from the mantle (e.g. Clark et al., 2011; Romer and Kroner, 2016). It is thus noteworthy that most of the Sn(–W) deposits of the Nanling region are concentrated close to the Chenzhou–Linwu Fault, which marks the suture between the Yangtze and Cathaysia blocks (Wang et al., 2003) and was a location of intense crust-mantle interaction in the Late Jurassic (Zhu et al., 2006; Li et al., 2009; Zhao et al., 2017). The Late Jurassic Sn-related granites along the Chenzhou-Linwu Fault are members of an A-type granite suite that were the products of the hybridization of anatectic granitic and mantle-derived mafic magmas (Zhu et al., 2006, 2008; Jiang et al., 2008; Huang et al., 2011; Shu et al., 2011; Zhao et al., 2012; Chen et al., 2013; Chen et al., 2016; Zhang et al., 2016). Several lines of evidence suggest that there was injection of mantle-derived melt along the Chenzhou–Linwu Fault during the Late Jurassic, which provided a highly focussed heat source. These lines of evidence are: (i) the Sr-Nd isotopic composition of the Late Jurassic Sn(-W)-mineralized granites is displaced from the field of the basement rocks of the Nanling Region toward higher εNd_{155} and lower $^{87}Sr/^{86}Sr$ values (Fig. 9), indicating that these granites cannot have been derived from the basement rocks alone; (ii) fine-grained mafic enclaves with acicular apatite and xenocrysts of K-feldspar and plagioclase, which occur in some of the Late Jurassic Sn(-W)-related granites, characterize the mingling and mixing of a mafic magma with local crustal melts (Vernon, 1986); (iii) their relatively depleted whole–rock Sr–Nd and zircon Hf–O isotope ratios indicate a mantle source for the mafic melts (Fig. 9, Zhu et al., 2006; Li et al., 2009; Zhao et al., 2012) and; (iv) there are coeval basalts in the region (Fig. 1B, Wang et al., 2003; Li et al., 2004). Heat from the injection of mantle-derived magmas is interpreted to have caused anatexis of the crust at higher temperature than from internal heating alone, allowing for the mobilization of Sn and W into the crustal melts. Although we cannot exclude the possibility that there was a contribution of other basement rocks to the magma that produced the Sn-mineralized granite, the Hehuaping Sn-mineralized granite and the Wangxianling W-mineralized granite are most likely to have been derived from the same protolith, which experienced magma extraction as a result of muscovite-controlled melting during the Late Triassic. Melting of the restite generated a Sn-enriched but W-poor magma and led to superposition of the Hehuaping Sn mineralization on earlier Triassic W mineralization in the Wangxianling area.

7 Conclusions

Zircon U–Pb and molybdenite Re–Os ages show that W and Sn mineralization in the Wangxianling ore field are related to separate intrusions that were emplaced in the Late Triassic (~220 Ma) and the Late Jurassic (~155 Ma), respectively. Both the Triassic and Jurassic granites are characterized by low oxygen fugacity. The Triassic granites, which are associated with W deposits, formed from magmas generated at low temperature (743 ± 15 °C) by muscovite-dehydration melting, whereas the Sn-mineralized Jurassic granites formed from higher temperature magmas (806 ± 19 °C) generated by biotite-dehydration melting that released both Sn and W into the magma. Because of the depletion of the protolith in W due to magma extraction in the Triassic, the Jurassic magmas were enriched in Sn relative to W. The difference in the temperature of partial melting of the protoliths in the Triassic and the Jurassic appears to have been the main reason for the temporal decoupling of W and Sn mineralization in the Wangxianling area. The different maximum temperatures reached during the Triassic and Jurassic magmatic events reflect different tectonic settings. In the Late Triassic, W granites formed in response to the collision between the Indochina Block and the South China Block. Crust-mantle interaction was weak and the maximum temperature attained was sufficient to mobilize W but not Sn into the magma, promoting the development of W mineralization. In the Late Jurassic, the involvement of mantle-derived juvenile material provided the heat for high-temperature melting that mobilized Sn into the magma and allowed for the formation of Jurassic granite-related Sn(–W) deposits. The hypothesis proposed above, invoking different temperatures of melting of the same protolith to explain separate mobilization of Sn and W, is potentially applicable to other Sn-W metallogenic provinces where Sn and W deposits are temporally separated.

Acknowledgements

This research was supported financially by the National Natural Science Foundation of China (41822304, 41672095). We thank editor Larry Meinert, reviewer Robin Shail, and an anonymous reviewer for their constructive comments, which significantly improved the manuscript.

References

Audétat, A., Gunther, D., and Heinrich, C.A., 2000a, Magmatic-hydrothermal evolution in a Fractionating granite: A microchemical study of the Sn–W–F mineralized Mole Granite (Australia): Geochimica et Cosmochimica Acta, v. 64, p. 3373–3393.

Audétat, A., Gunther, D., and Heinrich, C.A., 2000b, Causes for largescale metal zonation around mineralized plutons: Fluid inclusion LA–ICP–MS evidence from the Mole Granite, Australia: Economic Geology, v. 95, p. 1563–1581.

Baker, T., Pollard, P., Mustard, R., Mark, G., and Graham, J., 2005, A comparison of granite-related tin, tungsten, and gold–bismuth deposits: implication for exploration: Society of Economic Geologists, v. 61, p. 5–17.

Blevin, P.L., and Chappell, B.W., 1992, The role magma sources, oxidation states and fractionation in determining the granite metallogeny of eastern Australia: Transactions of the Royal Society of Edinburgh: Earth and Environmental Science, v. 83, p. 305–316.

Blevin, P.L., Chappell, B.W., and Allen, C.M., 1996, Intrusive metallogenic provinces in eastern Australia based on granite source and composition: Transactions of the Royal Society of Edinburgh: Earth Sciences, v. 87, p. 281–290.

Brown, T., and Pitfield, P., 2014, Tungsten, in Gunn, G., ed., Critical metals handbook: Oxford, John Wiley and Sons, p. 385-409.

Carter, A., Rogues, D., Bristar, C., and King, P., 2001, Understanding Mesozoic accretion in South–east Asia: Significance of Triassic thermotectonism (Indosinian orogeny) in Vietnam: Geology, v. 29, p. 211–214.

Chappell, B.W., Bryant, C.J., Wyborn, D., White, A.J.R., and Williams, I.S., 1998. High- and low-tempreature granites: Resource Geology, v. 48, p. 225-236.

Chappell, B.W., White, A.J.R., Williams, I.S., Wyborn, D., and Wyborn, L.A.I., 2000. Lachlan Fold Belt granites revisited: High- and low-temperature granites and and their implications: Australian J. Earth Sciences, v. 47, p. 123-138.

Chen, J.F., and Jahn, B.M., 1998, Crustl evolution of southeastern China: Nd and Sr isotopic evidence: Tectonophysics, v. 284, p. 101–133.

Clark, C., Fitzsimmons, I.C.W., and Healy, D., 2011, How does the continental crust get really hot? : Elements, v. 7, p. 235–240.

Du, A.D., Wu, S.Q., Sun, D.Z., Wang, S.X., Qu, W.J., Markey, R., Stein, H., Morgan, J., and Malinovskiy, D., 2004, Preparation and certification of Re–Os dating reference materials: Molybdenites HLP and JDC: Geostandards and Geoanalytical Research, v. 28, p. 41–52.

Du, Y., Shao, Y.J., Luo, X.Y., Guo, A.M., Huang, G.F., Tian, L., Wang, J.Y., and Chen, B.H., 2015, Geological Features and Genesis of Tianmuchong pollymetallic tungsten–tin Deposit in Guiyang County, Hunan Province: Geology and Mineral Resources of South China, v. 31, p. 354–367 (in Chinese with English abstract).

Gardiner, N.J., Hawkesworth, C.J., Robb, L.J., Whitehouse, M.J., Roberts, N.M.W., Kirkland, C.L., and Evans, N.J., 2017, Contrasting granite metallogeny through the zircon record: a case study from Myanmar: Scientific Reports, v. 7, p. 748.

Gardiner, N.J., Searle, M.P., morley, C.K., Robb, L.J., Whitehouse, M.J., Roberts, N.M.W., Kirkland, C.L., and Spencer, C.J., 2018, The crustal architecture of Myanmar imaged through zircon U-Pb, Lu-Hf and O isotopes: Tectonic and metallogenic implications: Gondwana Research, v. 62, p. 27-60.

Hoskin, P.W., and Schaltegger, U., 2003, The composition of zircon and igneous and metamorphic petrogenesis: Reviews in Mineralogy and Geochemistry, v. 53, p. 27–62.

Hou, K.J., Li, Y.H., and Tian, Y.R., 2009, In situ U–Pb zircon dating using laser ablation–multi–ion counting–ICP–MS: Mineral Deposits, v. 28, p.481–492 (in Chinese with English abstract).

Hou, M.S., Tian, X.F., He, Z.S., and Chen, Z.Q., 2015, Geological characteristics and genesis of Shuiyuanshan weathering eluvial clay-type tungsten deposit, Chenzhou, Hunan Province: Geology and Mineral Resources of South China, v. 31, p. 176–181 (in Chinese with English abstract).

Hu, G.R., 1998, Study on geochemistry, isotopic chronology and metamorphic P–T–t path of metamorphic rock belt in central Jiangxi: PhD Thesis, Nanjing University, China.

Hu, R.Z., and Zhou, M.F., 2012, Multiple Mesozoic mineralization events in South China–an introduction to the thematic issue: Mineralium Deposita, v. 47, p. 579–588.

Hu, R.Z., Wei, W.F., Bi, X.W., Peng, J.T., Qi, Y.Q., Wu, L.Y., and Chen, Y.W., 2012, Molybdenite Re–Os and muscovite $^{40}Ar/^{39}Ar$ dating of the Xihuashan tungsten deposit, central Nanling district, South China: Lithos, v. 150, p. 111–118.

Hu, R.Z., Chen, W.T., Xu, D.R., and Zhou, M.F., 2017, Reviews and new metallogenic models of mineral deposits in South China: An introduction: Journal of Asian Earth Sciences, v. 137, p. 1–8.

Huang, H.Q., Li, X.H., Li, W.X., and Li, Z.X., 2011, Formation of high δ18O fayalite-bearing A-type granite by hightemperature melting of granulitic metasedimentary rocks, southern China: Geology, v. 39, p. 903-906.

Huang, W.T., Wu, J., Zhang, J., Liang, H.Y., and Qiu, X.L., 2016, Geochemistry and Hf–Nd isotope characteristics and forming processes of the Yuntoujie granites associated with W–Mo deposit, Guangxi, South China: Ore Geology Reviews, v. 81, p. 953–964.

Ishihara, S., 1981, The granitoid series and mineralization: Economic Geology, v. 75, p. 458–484.

Ishihara, S., Hashimoto, M., and Machida, M., 2000, Magnetite/Ilmenite-series Classification and Magnetic Susceptibility of the Mesozoic–Cenozoic Batholiths in Peru: Resource Geology, v. 50, p. 123–129.

Jiang, Y.H., Ling, H.F., Jiang, S.Y., Shen, W.Z., Fan, H.R., and Ni, P., 2006, Trace element and Sr–Nd isotope geochemistry of fluorite from the Xiangshan uranium deposit, southeast China: Economic Geology, v. 101, p. 1613–1622.

Jiang, Y.H., Jiang, S.Y., Dai, B.Z., Liao, S.Y., Zhao, K.D., and Ling, H.F., 2009, Middle to late Jurassic felsic and mafic magmatism in southern Hunan Province, southeast China: Implications for a continental arc to rifting: Lithos, v. 107, p. 185–204.

Lehmann, B., 1990, Metallogeny of tin: Berlin, Springer, 211 p.

Li, X.H., Li, W.X., Wang, X.C., Li, Q.L., Liu, Y., and Tang, G.Q., 2009, Role of mantle-derived magma in genesis of early Yanshanian granites in the Nanling Range, South China: in situ zircon Hf–O isotopic constraints: Science in China series D: Earth Sciences, v. 52, p. 1262–1278.

Liang, X.Q., Dong, C.G., Jiang, Y., Wu, S.C., Zhou, Y., Zhu, H.F., Fu, J.G., Wang, C., and Shan, Y.H., 2016. Zircon U–Pb, molybdenite Re–Os and muscovite Ar–Ar isotopic dating of the Xitian W–Sn polymetallic deposit, eastern Hunan Province, South China and its geological significance: Ore Geology Reviews, v. 78, p. 85–100.

Linnen R. L., Pichavant M., Holtz F., and Burgess S., 1995, The effect of fO_2 on the solubility, diffusion, and speciation of tin in haplogranitic melt at 850 °C and 2 kbar: Geochimica et Cosmochimica Acta, v. 59, p. 1579–1588.

Liu, Y.S., Hu, Z.C., Gao, S., Günther, D., Xu, J., Gao, C.G., and Chen, H.H., 2008, In situ analysis of major and trace elements of anhydrous minerals by LA–ICP–MS without applying an internal standard: Chemical Geology, v. 257, p. 34–43.

Ludwig, K.R., 2001, User's manual for isoplot/ex, v2.49, a geochronological toolkit for Microsoft Excel: Geochronological Center Special Publication, p. 1–58.

Ludwig, K.R., 2003, User's Manual for Isoplot/Ex. Version 3.00: a geochronological toolkit for Microsoft Excel: Berkeley Geochronology Center Special Publication, Berkeley, p. 1–70.

Mao, J.W., Xie, G.Q., Guo, C.L., and Chen, Y.C., 2007, Large-scale tungsten–tin mineralization in the Nanling region, South China: Metallogenic ages and corresponding geodynamic processes: Acta Petrologica Sinica, v. 23, p. 2329–2338 (in Chinese with English abstract).

Mao, J.W., Pirajno, F., and Cook, N., 2011, Mesozoic metallogeny in East China and corresponding geodynamic settings–an introduction to the special issue: Ore Geology Reviews, v. 43, p. 1–7.

Mao, J.W., Cheng, Y.B., Chen, M.H., and Franco, P., 2013, Major types and time–space distribution of Mesozoic ore deposits in South China and their geodynamic settings: Mineralium Deposita, v. 48, p. 267–294.

Mao, J.W., Ouyang, H.G., Song, S.W., Santosh, M., Yuan, S.D., Z.H. Zhou, Zheng, W., Liu, H., Liu, P., Cheng, Y.B., Chen, M.H., 2019. Geology and metallogeny of tungsten and tin deposits in China. Society of Economic Geologists Special Publication: 22, p. 441-482.

Miller, C.F., McDowell, S.M., and Mapes, R.W., 2003, Hot and cold granites? Implications of zircon saturation temperatures and preservation of inheritance: Geology, v. 31, p. 529–532.

O'Neill, H.S.C., Berry, A.J., and Eggins, S.M., 2008, The solubility and oxidation state of tungsten in silicate melts: implications for the comparative chemistry of W and Mo in planetary differentiation processes: Chemical Geology, v. 255, p. 346–359.

Richards, J.P., 2015, The oxidation state, and sulfur and Cu contents of arc magmas: implications for metallogeny: Lithos, v. 233, p.27–45.

Romer, R.L., and Kroner, U., 2015, Sediment and weathering control on the distribution of Paleozoic magmatic tin–tungsten mineralization: Mineralium Deposita, v. 50, p. 327–338.

Romer, R.L., and Kroner, U., 2016, Phanerozoic tin and tungsten mineralization—tectonic controls on the distribution of enriched protoliths and heat sources for crustal melting: Gondwana Research, v. 31, p.60–95.

Sato, K., 2012, Sedimentary crust and metallogeny of granitoid affinity: implications from the geotectonic histories of the Circum–Japan Sea Region, Central Andes and southeastern Australia: Resource Geology, v. 62, p. 329–351.

Schmidt, C., Romer, R.L., Wohlgemuth-Ueberwasser, C., and Appelt, O. 2020, Partitioning of Sn and W between granitic melt and aqueous fluid: Ore Geology Reviews, v. 117, p. 103263.

Simons, B., Shail, R.K., and Andersen, J.C., 2016, The petrogenesis of the Early Permian Variscan granites of the Cornubian batholith: Lower plate post-collisional peraluminous magmatism in the Rhenohercynian zone of SW England: Lithos, v. 260, p. 76–94.

Simons, B., Andersen, J.C., Shail, R.K., and Jenner, F.E., 2017, Fractionation of Li, Be, Ga, Nb, Ta, In, Sn, Sb, W and Bi in the peraluminous Early Permian Variscan granites of the Cornubian Batholith: precursor processes to magmatic-hydrothermal mineralization: Lithos, v. 278, p. 491–512.

Sinclair, W.D., 2007, Porphyry deposits. In: Goodfellow, W.D. (Ed.), Mineral Deposits of Canada: A Synthesis of Major Deposit-Types, District Metallogeny, the Evolution of Geological Provinces, and Exploration Methods. Geological Association of Canada, Mineral Deposits Division, Special Publication 5, p. 223–243.

Smoliar, M.I., Walker, R.J., and Morgan, J.W., 1996, Re–Os ages of group IIA, IIIA, IVA, and IVB iron meteorites: Science, v. 271, p. 1099–1102.

Song, S.W., Mao, J.W., Zhu, Y.F., Yao, Z.Y., Chen, G.H., Rao, J.F., and Ouyang, Y.P., 2018, Partial-melting of fertile metasedimentary rocks controlling the ore formation in the Jiangnan porphyry-skarn tungsten belt, south China: A case study at the giant Zhuxi W-Cu skarn deposit: Lithos, v. 304–307, p. 180–199.

Su, H.Z., 2017, The petrogenesis studies of the Mesozoic Xiangyuan tungsten–tin deposit and related granites in Hunan Province: Master thesis, China University of Geosciences, Beijing (in Chinese with English abstract).

Vernon, R.H., 1986. K-feldspar megacrysts in granites—phenocrysts, not porphyroblasts. Earth-Science Reviews, v. 23, p. 1–63.

Viruete, J.E., Indares, A., and Arenas, R., 2000, P–T paths derived from garnet growth zoning in an extensional setting: an example from the Tormes gneiss dome (Iberian massif, Spain): Journal of Petrology, v. 41, p. 1489–1515.

Wang, Y.J., Fan, W.M., Guo, F., Peng, T.P., and Li, C.W., 2003, Geochemistry of Mesozoic mafic rocks adjacent to the Chenzhou–Linwu fault, South China: implications for the lithospheric boundary between the Yangtze and Cathaysia blocks: International Geology Review, v. 45, p. 263–286.

Wang, Y.J., Fan, W.M., Sun, M., Liang, X.Q., Zhang, Y.H., and Peng, T.P., 2007, Geochronological, geochemical and geothermal constraints on petrogenesis of the Indosinian peraluminous granites in the South China Block: a case study in the Hunan Province: Lithos, v. 96, p. 475–502.

Wang, Y.J., Fan, W.M., Zhang, G.W., and Zhang, Y.H., 2013, Phanerozoic tectonics of the South China Block: Key observations and controversies: Gondwana Research, v. 23, p. 1273–1305.

Watson, E.B., and Harrison, T. M., 1983, Zircon saturation revisited: temperature and composition effects in a variety of crustal magma types: Earth and Planetary Science Letters, v. 64, p. 295–304.

Wei, Z.Y., Yu, J.H., Wang, L.J., and Shu, L.S., 2009, Geochemical features and tectonic significances of Neoproterozoic metasedimentary rocks from Nanling Range: Geochimica, v. 38, p. 1–19 (in Chinese with English abstract).

White, R.W., Powell, R., and Holland, T.J.B., 2007, Progress relating to calculation of partial melting equilibria for metapelites: Journal of Metamorphic Geology, v. 25, p. 511-527, doi:10.1111/j.1525-1314.2007.00711.x.

White, L.T. and Ireland, T.R., 2012. High-uranium matrix effect in zircon and its implications for SHRIMP U–Pb age determinations: Chemical Geology, v. 306–307, p. 78–91.

Wolf, M., Romer, R.L., Franz, L., and López-Moro, F.J., 2018, Tin in granitic melts: The role of melting temperature and protolith composition: Lithos, v. 310–311, p. 20–30.

Wu, F.Y., Sun, D.Y., Li, H.M., Jahn, B-M., and Wilde, S., 2002, A–type granites in northeastern China: age and geochemical constraints on their petrogenesis: Chemical Geology, v.187, p.143–173.

Wu, J., Liang, H.Y., Huang, W.T., Wang, C.L., Sun, W.D., Sun, Y.L., Li, J., Mo, L.H., and Wang, X.Z., 2012, Indosinian isotope ages of plutons and deposits in southwestern Miaoershan–Yuechengling, northeastern Guangxi and implications on Indosinian mineralization in South China: Chinese Science Bulletin, v. 57, p. 1024–1035.

Wu, S.N., 2006, Geological characteristics of the Hehuaping tin-polymetallic deposit in Chenzhou, Hunan Province: Mineral Resources and Geology, v. 20, p. 43–46 (in Chinese with English abstract).

Xuan, Y.S., Yuan, S.D., Yuan, Y.B., and Mi, J.R., 2014, Zircon U–Pb age, geochemistry and petrogenesis of Jianfengling pluton in southern Hunan Province: Mineral Deposits, v. 33, p. 1379–1390 (in Chinese with English abstract).

Yao, Y., Chen, J., Lu, J.J., Wang, R.C., and Zhang, R.Q., 2014, Geology and genesis of the Hehuaping magnesian skarn-type cassiterite-sulfide deposit, Hunan Province, Southern China: Ore Geology Reviews, v. 58, p.163–184.

Yu J.H., Wei Z.Y., Wang L.J., Wang R.C., Jiang S.Y., Shu L.S., and Sun T., 2006, Cathaysia Block: A young continent composed of ancient materials: Geological Journal of China Universities, v. 12, p. 440–447. (in Chinese with English abstract)

Yu, J.H., O'Reilly, S.Y., Wang, L.J., Griffin, W.L., Zhou, M.F., Zhang, M., and Shu, L.S., 2010, Components and Episodic growth of Precambrian crust in the Cathaysia Block, South China:

evidence from U–Pb ages and Hf isotopes of zircons in Neoproterozoic sediments: Precambrian Research, v. 181, p. 97–114.

Yuan, S.D., Peng, J.T., Hao, S., Li, H.M., Geng, J.Z., and Zhang, D.L., 2011, In situ LA–MC–ICP–MS and ID–TIMS U–Pb geochronology of cassiterite in the giant Furong tin deposit, Hunan Province, South China: New constraints on the timing of tin-polymetallic mineralization: Ore Geology Reviews, v. 43, p. 235–242.

Yuan, S.D., Williams-Jones, A.E., Mao, J.W., Zhao, P.L., Yan, C., and Zhang, D.L., 2018, The origin of the Zhangjialong tungsten deposit, South China: implications for W–Sn mineralization in large granite batholiths: Economic Geology, v. 113, p. 1193–1208.

Yuan, S.D., Williams-Jones, A.E., Romer, R.L., Zhao, P.L., and Mao, J.W., 2019, Protolith-related thermal controls on the decoupling of Sn and W in Sn–W metallogenic provinces: insights from the Nanling region, China: Economic Geology, v. 114, p. 1005–1012.

Yuan, Y.B., Yuan, S.D., Mao, J.W., Zhao, P.L., Yan, C., Zhao, H.J., Zhang, D.L., Shuang, Y., and Peng, J.T. 2018, Recognition of Late Jurassic W–Sn mineralization and its exploration potential on the western margin of the Caledonian Guidong granite batholith, Nanling Range, South China: Geochronological evidence from the Liuyuan Sn and Zhuyuanli W deposits: Ore Geology Reviews, v. 93, p. 200–210.

Yuan, Z.X., Wu, L.S., Zhang, Z.Q., and Ye, X.J., 1991, Study on Sm–Nd and Rb–Sr isotopic age of the Mayuan Group in Northern Fujian: Acta Petrologica et Mineralogica, v. 10, p. 127–132 (in Chinese with English abstract).

Zhang, R.Q., Lu, J.J., Wang, R.C., Yang, P., Zhu, J.C., Yao, Y., Gao, J.F., Li, C., Lei, Z.H., Zhang, W.L., and Guo, W.M., 2015, Constraints of in situ zircon and cassiterite U–Pb, molybdenite Re–Os and muscovite ^{40}Ar–^{39}Ar ages on multiple generations of granitic magmatism and related W–Sn mineralization in the Wangxianling area, Nanling Range, South China: Ore Geology Reviews, v. 65, p. 1021–1042.

Zhang, R.Q., Lu, J.J., Wang, R.C., Yao, Y., Ding, T., Hu, J.B., and Zhang, H.F., 2016, Petrogenesis of and Sn-bearing granites and the mechanism of their metallogenic diversity in the Wangxianling area, southern Hunan Province: Geochimica, v. 45, p. 105–132 (in Chinese with English abstract).

Zhao, J.H., Zhou, M.F., Yan, D.P., Zheng, J.P., and Li, J.W., 2011, Reappraisal of the ages of Neoproterozoic strata in South China: No connection with the Grenvillian orogeny: Geology, v. 39, p. 299–302.

Zhao, K.D., Jiang, S.Y., Yang, S.Y., Dai, B.Z., and Lu, J.J., 2012, Mineral chemistry, trace elements and Sr–Nd–Hf isotope geochemistry and petrogenesis of Cailing and Furong granites and mafic enclaves from the Qitianling batholith in the Shi–Hang zone, South China: Gondwana Research, v. 22, p. 310–324.

Zhao, P.L., Yuan, S.D., Mao, J.W., Santosh M., Li C., and Hou K.J., 2016, Geochronological and petrogeochemical constraints on the skarn deposits in Tongshanling ore district, Southern Hunan Province: Implications for Jurassic Cu and W metallogenic events in South China: Ore Geology Reviews, v. 78, p. 120–137.

Zhao, P.L., Yuan, S.D., Mao, J.W., Yuan, Y.B., Zhao, H.J., Zhang, D.L., and Shuang, Y., 2018, Constraints on the timing and genetic link of the large-scale accumulation of proximal W–Sn–Mo–Bi and distal Pb–Zn–Ag mineralization of the world-class Dongpo orefield, Nanling Range, South China: Ore Geology Reviews, v. 95, p. 1140–1160.

Zhou, X.M., Sun, T., Shen, W.Z., Shu, L.S., and Niu, Y.L., 2006, Petrogenesis of Mesozoic granitoids and volcanic rocks in South China: a response to tectonic evolution: Episodes, v. 29, p. 26–33.

Zhu, J.C., Zhang, P.H., Xie, C.F., Zhang, H., and Yang, C., 2006, The Huashan–Guposhan A–type granitoid belt in the western part of the Nanling Mountains: petrology, geochemistry and genetic interpretations: Acta Geologica Sinica, v. 80, p. 529–542 (in Chinese with English abstract).

Zou, X.W., Cui, S., Qu, W.J., Bai, Y.S., and Chen, X.Q., 2009, Re–Os isotope dating of the Liguifu tungsten–tin polymetallic deposit in Dupangling area, Guangxi: Geology in China, v. 36, p. 837–844 (in Chinese with English abstract).

Figure captions

Fig. 1 The distribution of W and Sn deposits and associated granites in the Nanling region, South China (modified after Yuan et al., 2018).

Fig. 2A A simplified geological map of the Wangxianling area, showing the distribution of W and Sn deposits (modified after Zhang et al., 2015). Fig. 2B A simplified geological map of the Shuiyuanshan W deposit (modified after Zhang et al., 2015). Fig. 2C A profile along an exploration trench through the Shuiyuanshan W deposit (modified after Hou et al., 2015). The Wangxianling pluton constitutes of coarse- to medium- and fine-grained tourmaline two-mica granite phases, which are not distinguished in the geological map.

Fig. 3 Photographs of representative granite samples from the Wangxianling pluton (A–D) and Hehuaping pluton (E–F). (A) A photograph of a hand specimen and (B) photomicrograph (crossed nicols) of medium-grained tourmaline-bearing two-mica granite; (C) A photograph of a hand specimen and (D) photomicrograph (crossed nicols) of fine-grained tourmaline-bearing two-mica granite; (E) A photograph of a hand specimen and (F) photomicrograph (crossed nicols) of biotite granite from the Hehuaping Sn deposit. Bi = biotite, Kfs = K-feldspars, Mus = muscovite, Pl = plagioclase, Qtz = quartz, Tur = tourmaline.

Fig. 4 A simplified geological map (A) and cross section (B) of the Hehuaping Sn deposit (modified after Wu, 2006)

Fig. 5 Representative ore samples from the Shuiyuanshan W (A–F) and Hehuaping Sn deposits (G–H). (A) A hand specimen photograph and (B) photomicrograph (plane polarized light) of greisen-type scheelite ore; (C) A hand specimen photograph and (D) photomicrograph (reflected light) of molybdenite-bearing greisen ore; (E) A hand specimen photograph and (F) microphotograph (reflected light) of a wolframite-bearing quartz vein. (G) A hand specimen photograph and (H) photomicrograph (plane polarized light) of cassiterite–sulfide ore. Cst = cassiterite, Mol = molybdenite, Mt = magnetite, Mus = muscovite, Py = pyrite, Qtz = quartz, Sch = scheelite, Sp = sphalerite, Tur = tourmaline, Wol = wolframite.

Fig. 6 Concordia and isochron diagrams for zircon and molybdenite, respectively, from the Wangxianling area. Concodia diagram for LA–ICP–MS U–Pb zircon data of (A) a medium-grained tourmaline-bearing two-mica granite sample (SYS–9), (B) a fine-grained tourmaline-bearing Shuiyuanshan two-mica granite sample (SYS–3–3–4), and (C) a Hehuaping biotite granite sample (SYS–7). The insets show the apparent $^{206}Pb/^{238}U$ ages. (D) Re–Os isochron diagram for molybdenite sample SYS–8 from the greisen-type ore in the Shuiyuanshan W deposit. The inset shows the apparent $^{187}Os/^{187}Re$ ages. MSWD = mean square of weighted deviates.

Fig. 7 (A-B) Plots of Fe_2O_3/FeO versus SiO_2 and Rb/Sr for the Wangxianling and Hehuaping granites. (C-D) Variations of Sn and W concentration as a function of the degree of fractionation expressed as TiO_2 and Zr/Hf ratio for the Wangxianling and Hehuaping granite. The fields for the different types of granite-related mineralization in (A) and (B) are from Lehmann (1990), Sinclair (2007), and Blevin et al. (1996). The dashed line separating the magnetite and ilmenite series granites is from Ishihara et al. (2000).

Fig. 8 Plots of zircon saturation temperature (A-B), Ba/Pb ratio (C) and Al_2O_3/TiO_2 ratio (D) as a function of the degree of fractionation expressed as Zr/Hf and K/Rb ratio for the W-related Wangxianling granite and Sn-related Hehuaping granite. The dotted lines indicate the fractionation trends of the various granitic magmas

Fig. 9 The Sr–Nd isotopic compositions of the Hehuaping and Wangxianling granites. The whole–rock Sr–Nd isotopic compositions of Jurassic Daoxian basalt (~150 Ma, Fig. 1B, Jiang et al., 2009) and fine-grained mafic enclaves in Jurassic Sn granites (Huashan, Guposhan, Qitianling, Fig. 1B, Zhu et al., 2006; Zhao et al., 2012) are shown for comparison. The $^{87}Sr/^{86}Sr$ values are only shown for granite samples with a $^{87}Rb/^{86}Sr$ ratio < 20, as high Rb/Sr ratios in highly fractionated granite result in large uncertainties of the $^{87}Sr/^{86}Sr$ values (Wu et al., 2002). The Sr–Nd isotopic data of the metamorphic basement in the Nanling region are from Yuan et al. (1991), Hu et al. (1998) and Jiang et al. (2006). All the whole–rock Sr–Nd isotope in Fig. 9A were recalculated to 155 Ma.

Fig. 10 Plot of (A) zircon U–Pb age vs. whole–rock $\varepsilon_{Nd}(t)$ values and (B) zircon-saturation temperature vs. whole-rock $\varepsilon_{Nd}(t)$ values for Late Triassic W-related granites and Late Jurassic Sn(–W) granites in the western part of Nanling region. The data are from Appendix Tables A3 and A4. The Sr–Nd isotopic data for the metamorphic basement in the Nanling region are from Yuan et al. (1991), Hu (1998), and Jiang et al. (2006). All the whole-rock Nd isotope were recalculated to 155 Ma.

Appendix Fig. A1 Cathodoluminescence (CL) images of representative zircon crystals from the Wangxianling tourmaline-bearing two-mica granite (SYS-9 and SYS-3-3-4) and the Hehuaping biotite granite (SYS-7). Red full circles: LA–MC–ICP–MS spots for $^{206}Pb/^{238}U$ age determination. Age uncertainties are given at the 1σ level. Yellow dashed circles: LA–MC–ICP–MS mark analytical spots on inherited cores. Note the different scale bars of 50 and 100 μm, respectively, for zircon from different samples.

Appendix Fig. A2 Plots of zircon saturation temperature (T_{Zr} °C) versus Nb/Ta and Zr/Hf ratios for Late Triassic granites with associated W mineralization and Late Jurassic granites with associated Sn(–W)- mineralization in the western part of the Nanling region. The maximum zircon saturation temperature was taken to approximate the initial magma temperature (see Watson and Harrison, 1983). The Nb/Ta and Zr/Hf ratios are used as proxies for the degree of fractional crystallization. The locations of the granites are shown in Fig. 1.

Appendix Fig. A3 Pressure-temperature pseudosection for an average metapelitic composition modified from White et al. (2007). Quartz and ilmenite are stable phase in all the P-T field in the figure. g-garnet, opx-orthopyroxene, cd-cordierite, sp-spinel, ky/sill-aluminosilicate, bi-biotite, mu-muscovite, os-osumulite, ksp-K-feldspar, q-quartz, liq-silicate liquid, pl-plagioclase, mt-magnetite, ilm-ilmenite, hem-haematite, ru-rutile.

Table 1: Geological and geochronological data for representative Late Jurassic Sn(–W) and Late Triassic W deposits in the Nanling region, South China.

Appendix Table A1: LA–MC–ICP–MS U–Pb zircon data of tourmaline-bearing two-mica granite and biotite granite in the Wangxianling area, Nanling region, South China.

Appendix Table A2: Re–Os isotope data for molybdenite from the Shuiyuanshan W deposit, Nanling region.

Appendix Table A3: Geochemical and Nd isotopic data for the Late Jurassic Sn(–W)- and Late Triassic W-related granites in the western part of the Nanling region, South China.

Appendix Table A4: Whole–rock Sr–Nd isotope data for the Hehuaping granite and Triassic W-related granites in the western part of the Nanling region, South China.

Appendix Table A5: Partition coefficients for W and Sn between minerals and melt.

Appendix Material A1: Zircon-saturation thermometry used in this study and its application to evaluate the melting temperature of granite.

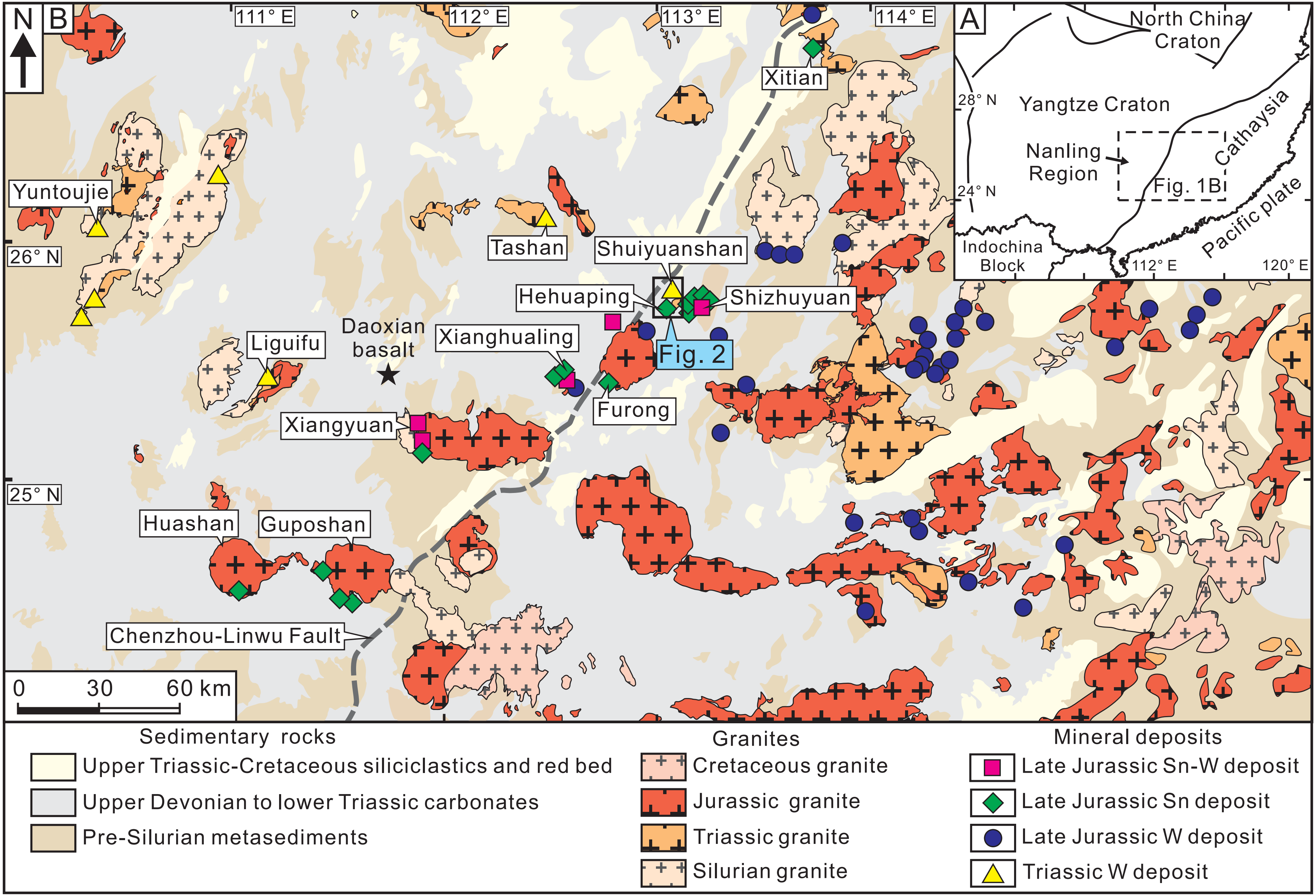
N
B
111° E
112° E
113° E
114° E
A
North China Craton
28° N
Yangtze Craton
Cathaysia
Nanling Region
Fig. 1B
24° N
Pacific plate
Indochina Block
112° E
120° E
Xitian
Yuntoujie
Tashan
Shuiyuanshan
26° N
Hehuaping
Shizhuyuan
Daoxian basalt
Liguifu
Xianghualing
Fig. 2
Furong
Xiangyuan
25° N
Huashan
Guposhan
Chenzhou-Linwu Fault
0 30 60 km
Sedimentary rocks
Upper Triassic-Cretaceous siliciclastics and red bed
Upper Devonian to lower Triassic carbonates
Pre-Silurian metasediments
Granites
Cretaceous granite
Jurassic granite
Triassic granite
Silurian granite
Mineral deposits
Late Jurassic Sn-W deposit
Late Jurassic Sn deposit
Late Jurassic W deposit
Triassic W deposit

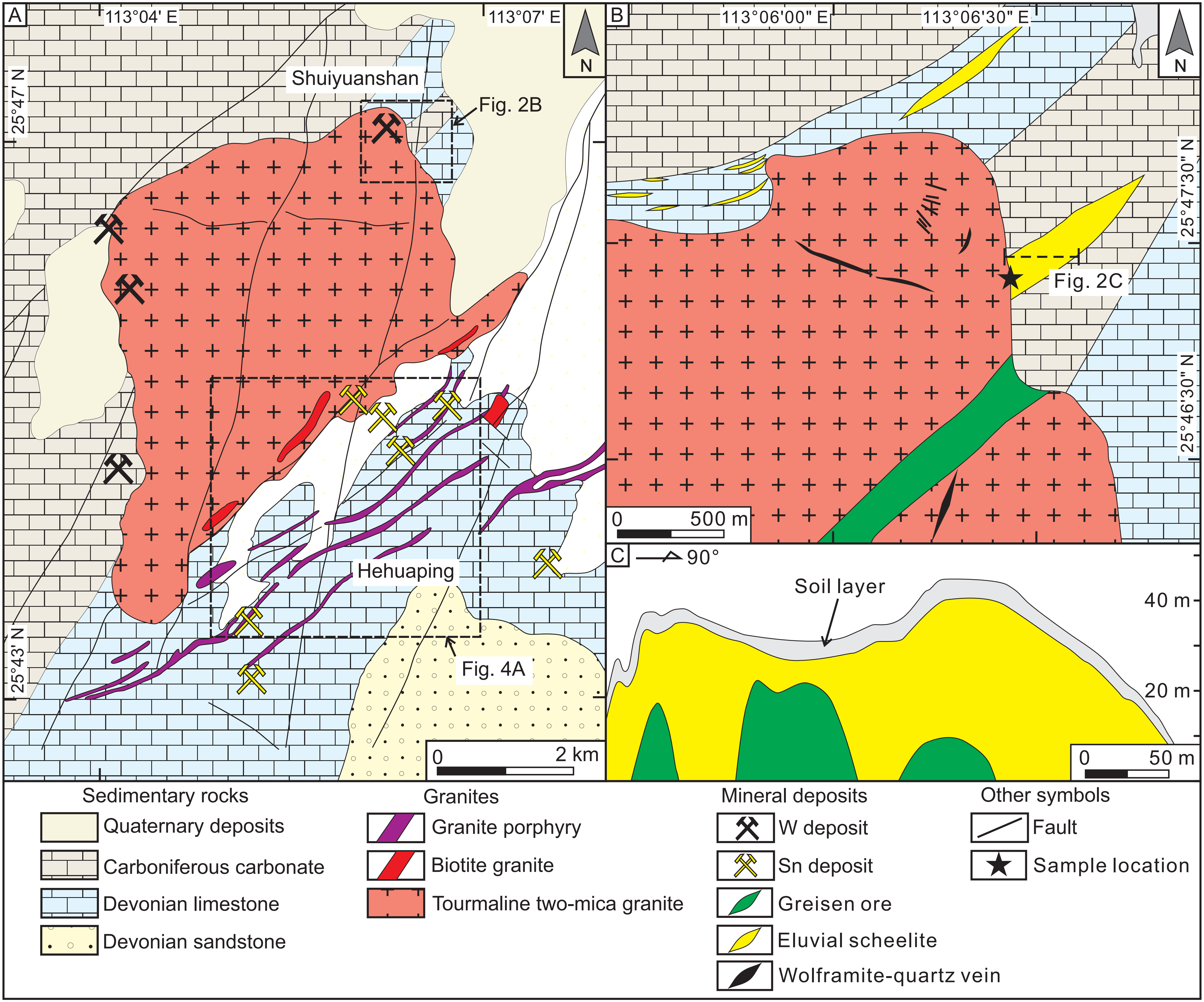
A
113°04' E
113°07' E
N
25°47' N
25°43' N
Shuiyuanshan
Fig. 2B
Hehuaping
Fig. 4A
0
2 km
B
113°06'00" E
113°06'30" E
25°47'30" N
25°46'30" N
Fig. 2C
0
500 m
C
90°
Soil layer
40 m
20 m
0
50 m
Sedimentary rocks
Quaternary deposits
Carboniferous carbonate
Devonian limestone
Devonian sandstone
Granites
Granite porphyry
Biotite granite
Tourmaline two-mica granite
Mineral deposits
W deposit
Sn deposit
Greisen ore
Eluvial scheelite
Wolframite-quartz vein
Other symbols
Fault
Sample location

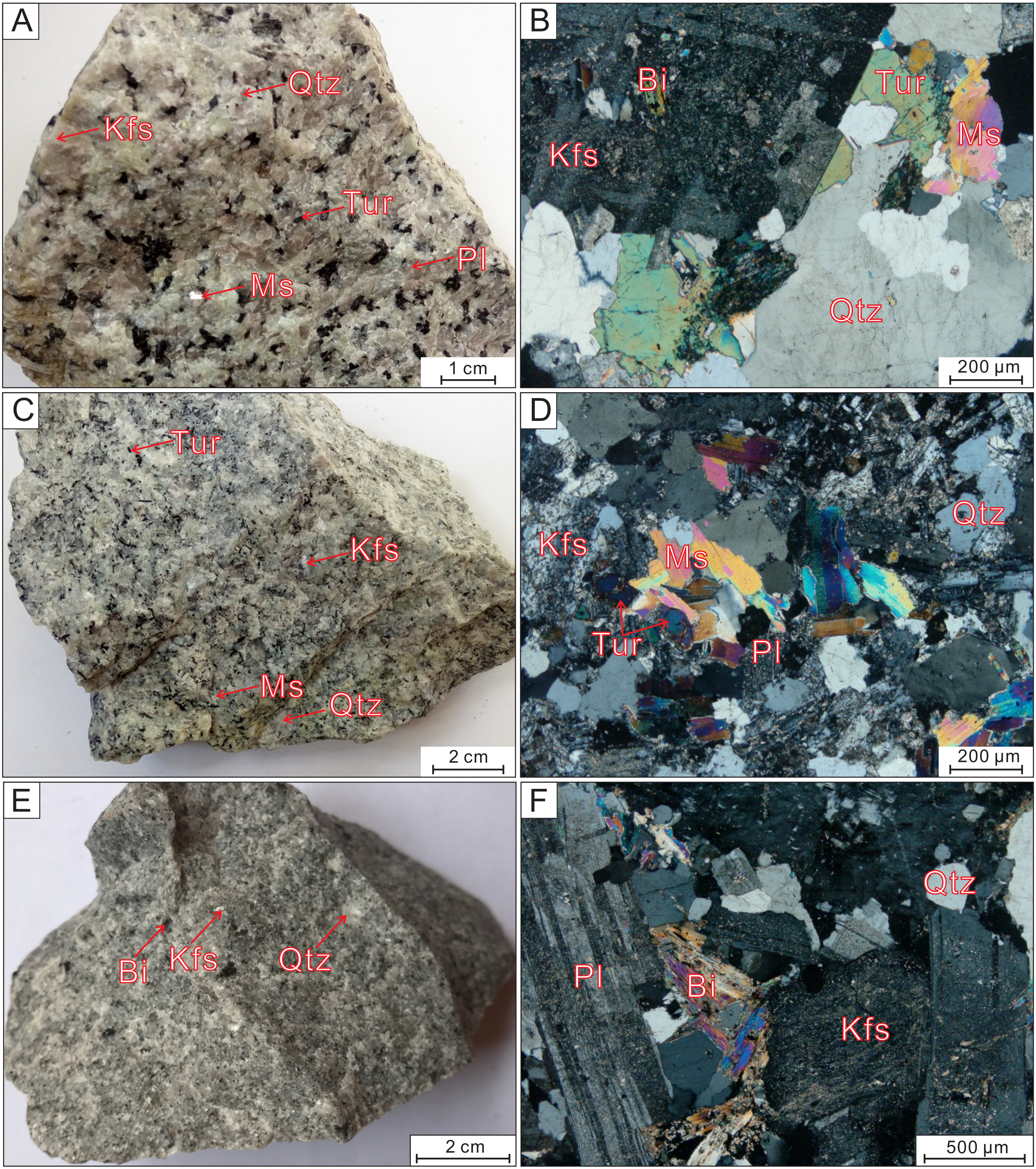
A
Qtz
Kfs
Tur
Pl
Ms
1 cm
B
Bi
Tur
Ms
Kfs
Qtz
200 μm
C
Tur
Kfs
Ms
Qtz
2 cm
D
Qtz
Kfs
Ms
Tur
Pl
200 μm
E
Bi
Kfs
Qtz
2 cm
F
Qtz
Pl
Bi
Kfs
500 μm

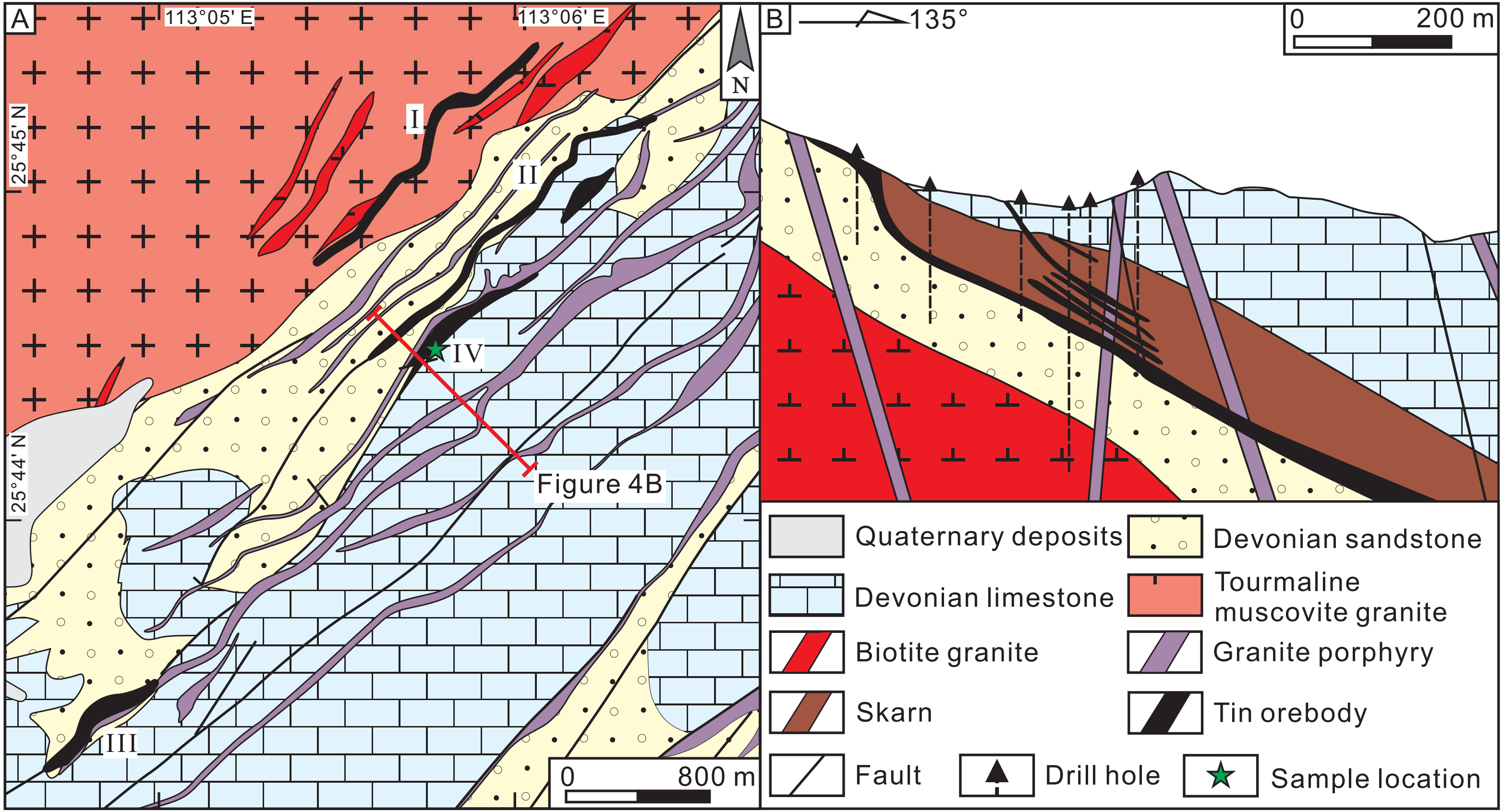

A
113°05' E
113°06' E
N
25°45' N
25°44' N
I
II
III
IV
Figure 4B
0
800 m
B
135°
0
200 m
Quaternary deposits
Devonian sandstone
Devonian limestone
Tourmaline muscovite granite
Biotite granite
Granite porphyry
Skarn
Tin orebody
Fault
Drill hole
Sample location

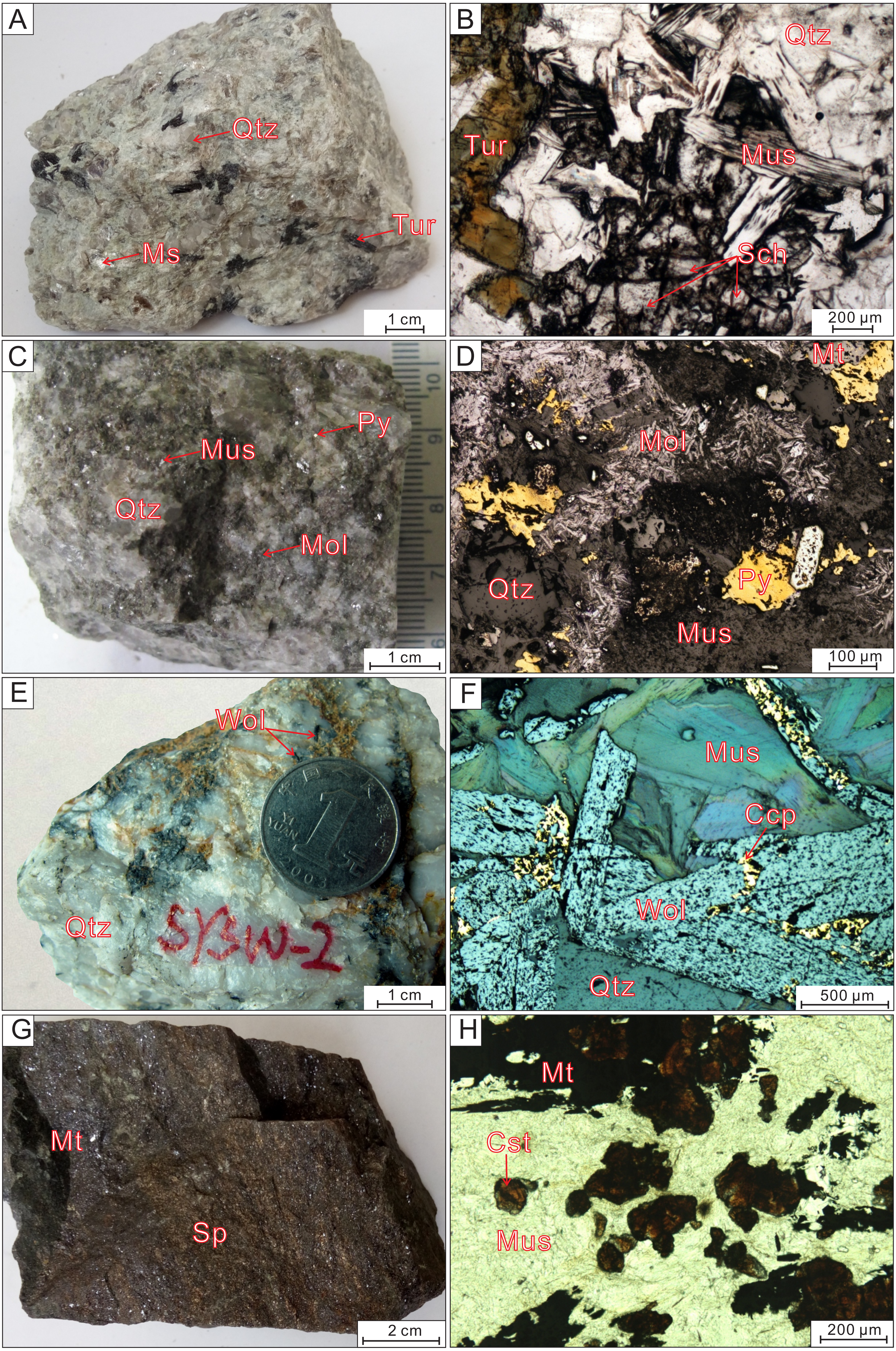
A
Qtz
Tur
Ms
1 cm
B
Qtz
Tur
Mus
Sch
200 μm
C
Py
Mus
Qtz
Mol
1 cm
D
Mt
Mol
Qtz
Py
Mus
100 μm
E
Wol
Qtz
SYSW-2
1 cm
F
Mus
Ccp
Wol
Qtz
500 μm
G
Mt
Sp
2 cm
H
Mt
Cst
Mus
200 μm

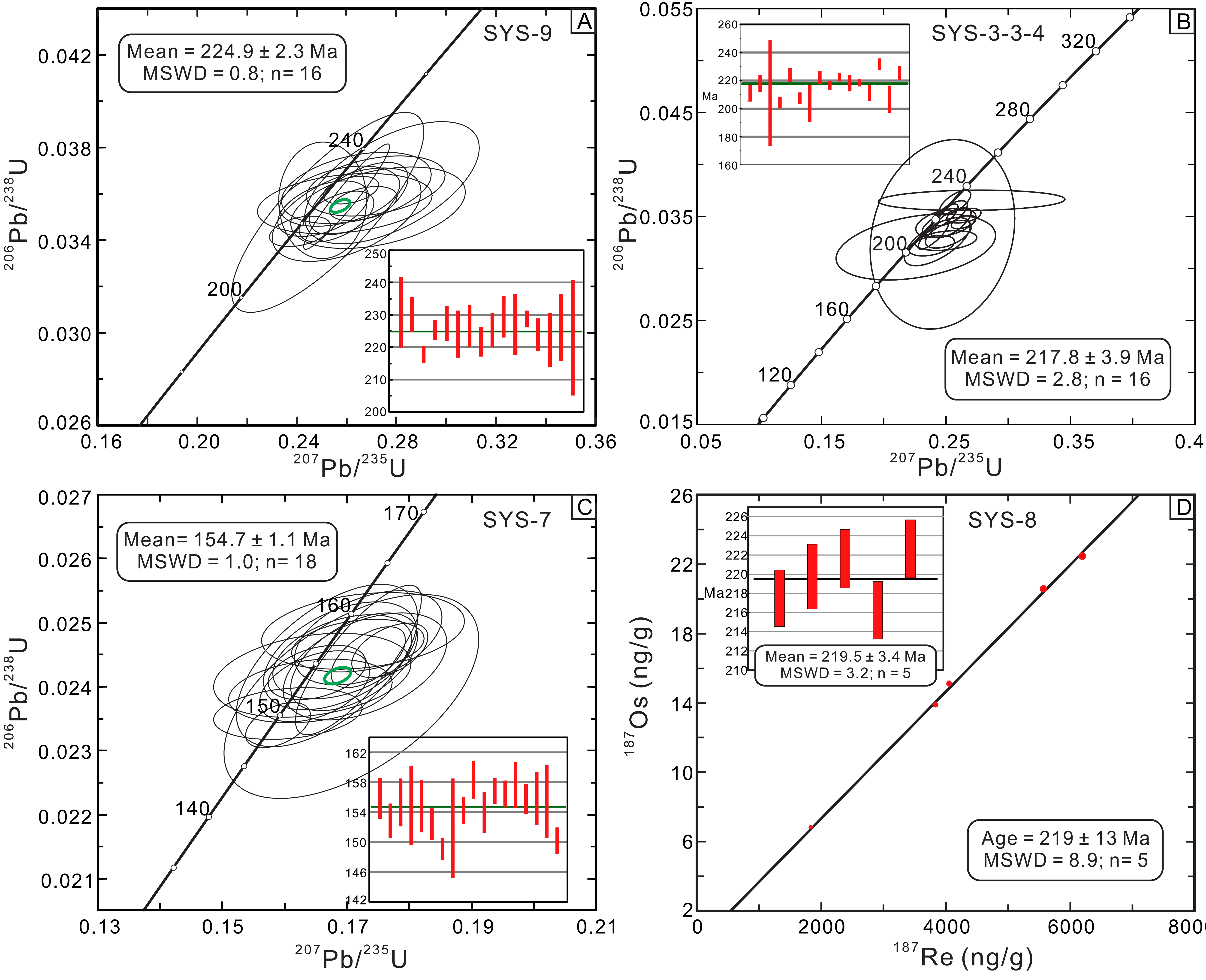

A
SYS-9
Mean = 224.9 ± 2.3 Ma
MSWD = 0.8; n= 16
$^{206}Pb/^{238}U$
$^{207}Pb/^{235}U$
B
SYS-3-3-4
Mean = 217.8 ± 3.9 Ma
MSWD = 2.8; n = 16
Ma
$^{206}Pb/^{238}U$
$^{207}Pb/^{235}U$
C
SYS-7
Mean= 154.7 ± 1.1 Ma
MSWD = 1.0; n= 18
$^{206}Pb/^{238}U$
$^{207}Pb/^{235}U$
D
SYS-8
Mean = 219.5 ± 3.4 Ma
MSWD = 3.2; n = 5
Ma
Age = 219 ± 13 Ma
MSWD = 8.9; n= 5
^{187}Os (ng/g)
^{187}Re (ng/g)

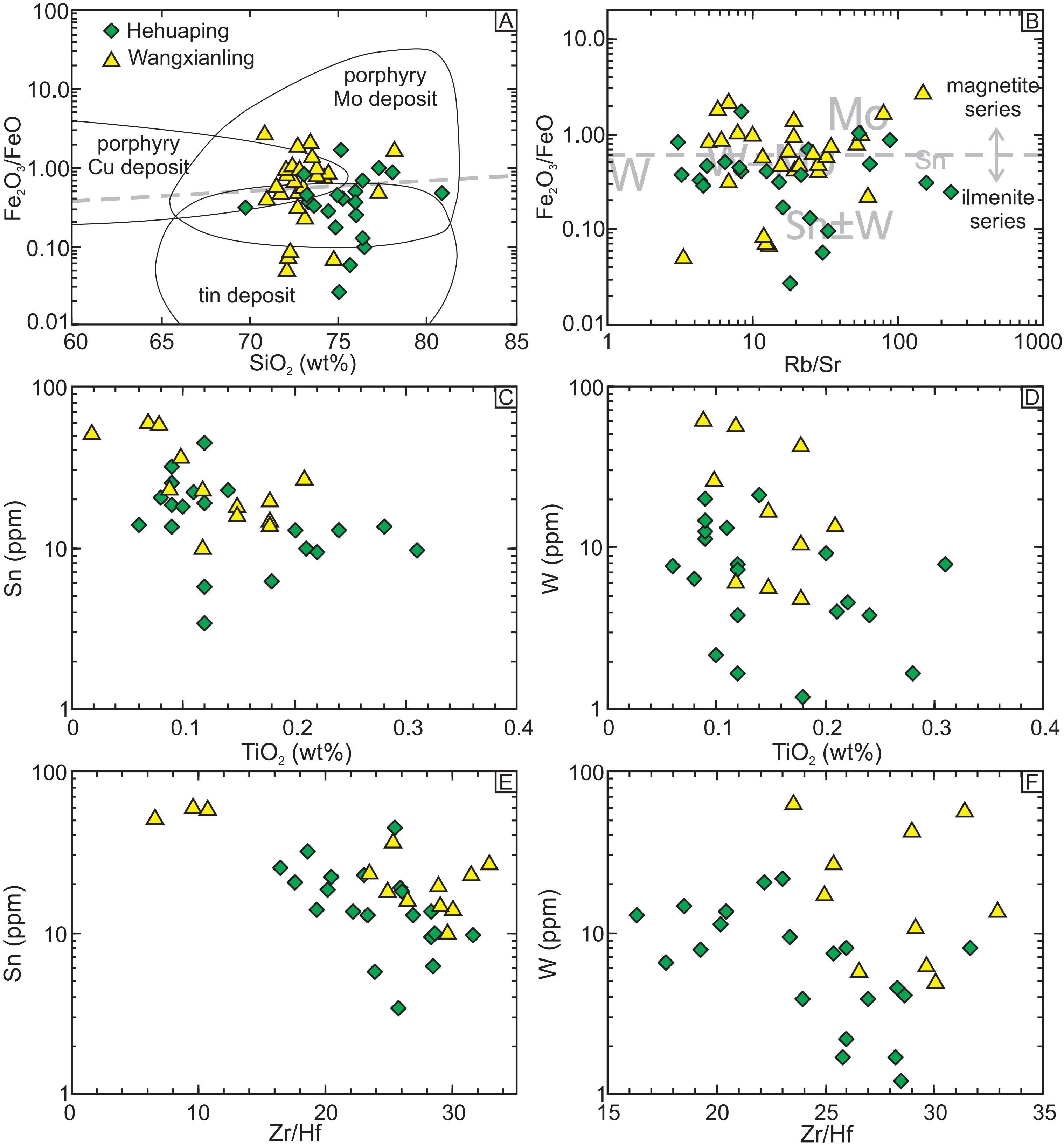

A
Hehuaping
Wangxianling
porphyry Mo deposit
porphyry Cu deposit
tin deposit
Fe_2O_3/FeO
SiO_2 (wt%)
B
magnetite series
ilmenite series
Mo
W
W+Mo
Sn
Sn±W
Rb/Sr
C
Sn (ppm)
TiO_2 (wt%)
D
W (ppm)
E
Zr/Hf
F

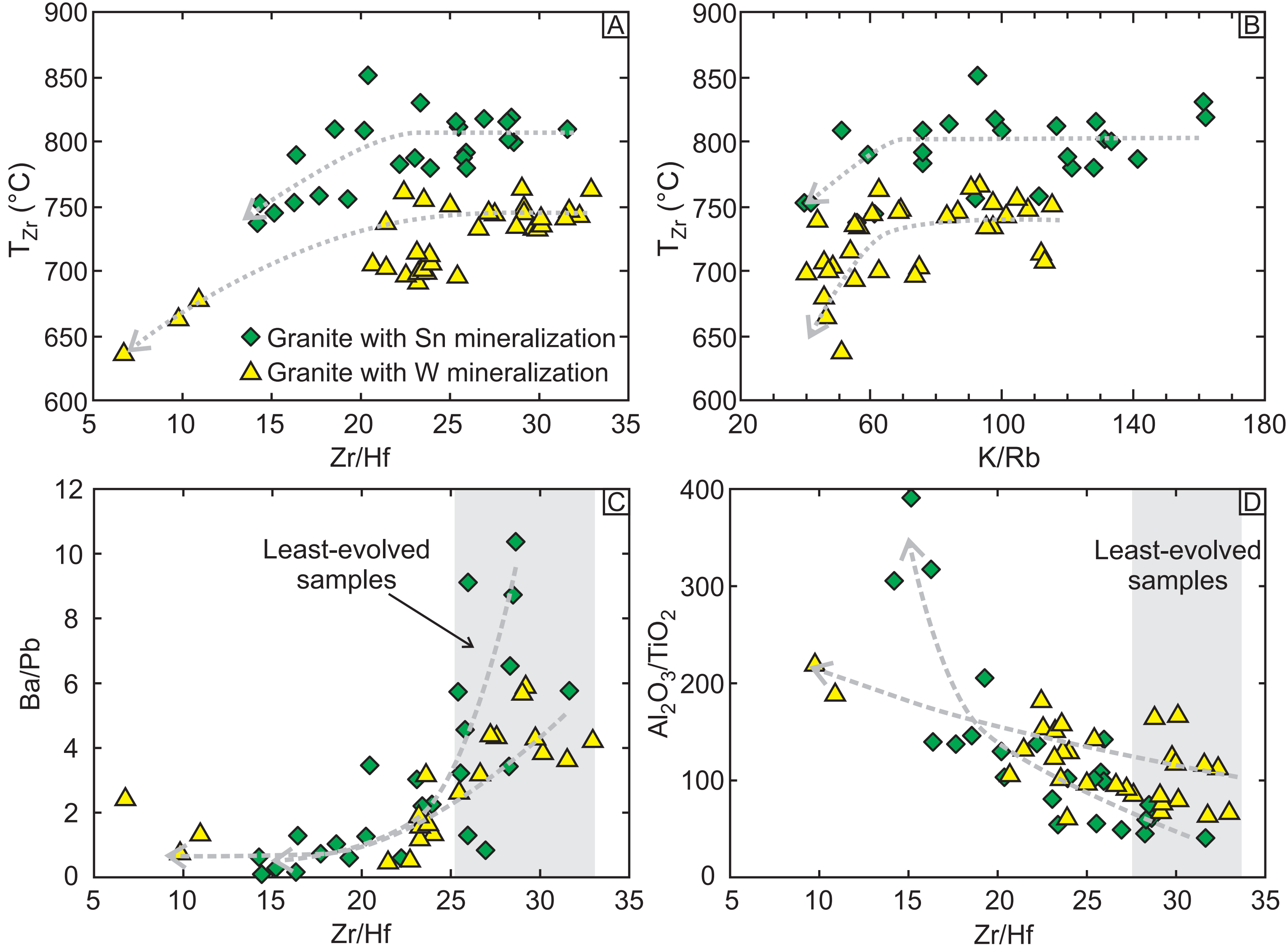

A
B
C
D
T_{Zr} (°C)
Zr/Hf
K/Rb
Ba/Pb
Al_2O_3/TiO_2
Granite with Sn mineralization
Granite with W mineralization
Least-evolved samples
Least-evolved samples
900
850
800
750
700
650
600
5
10
15
20
25
30
35
20
60
100
140
180
12
10
8
6
4
2
0
400
300
200
100

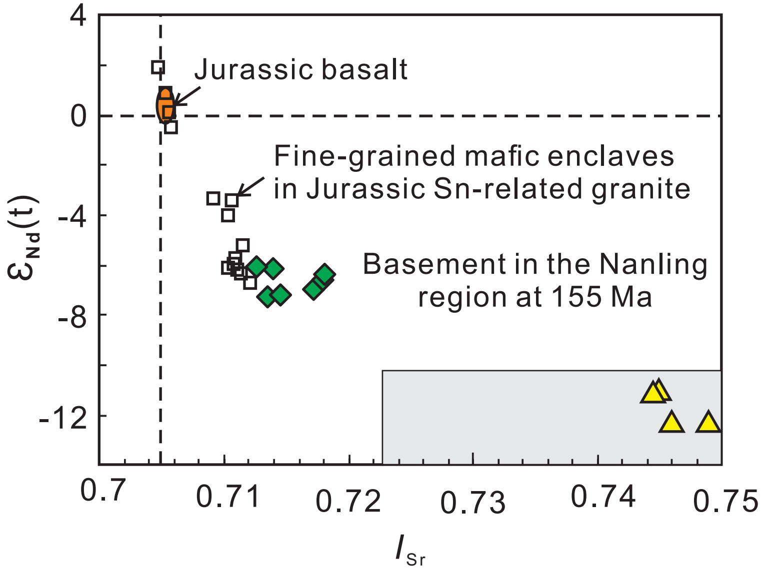
Jurassic basalt
Fine-grained mafic enclaves in Jurassic Sn-related granite
Basement in the Nanling region at 155 Ma
εNd(t)
ISr
4
0
-4
-8
-12
0.7
0.71
0.72
0.73
0.74
0.75

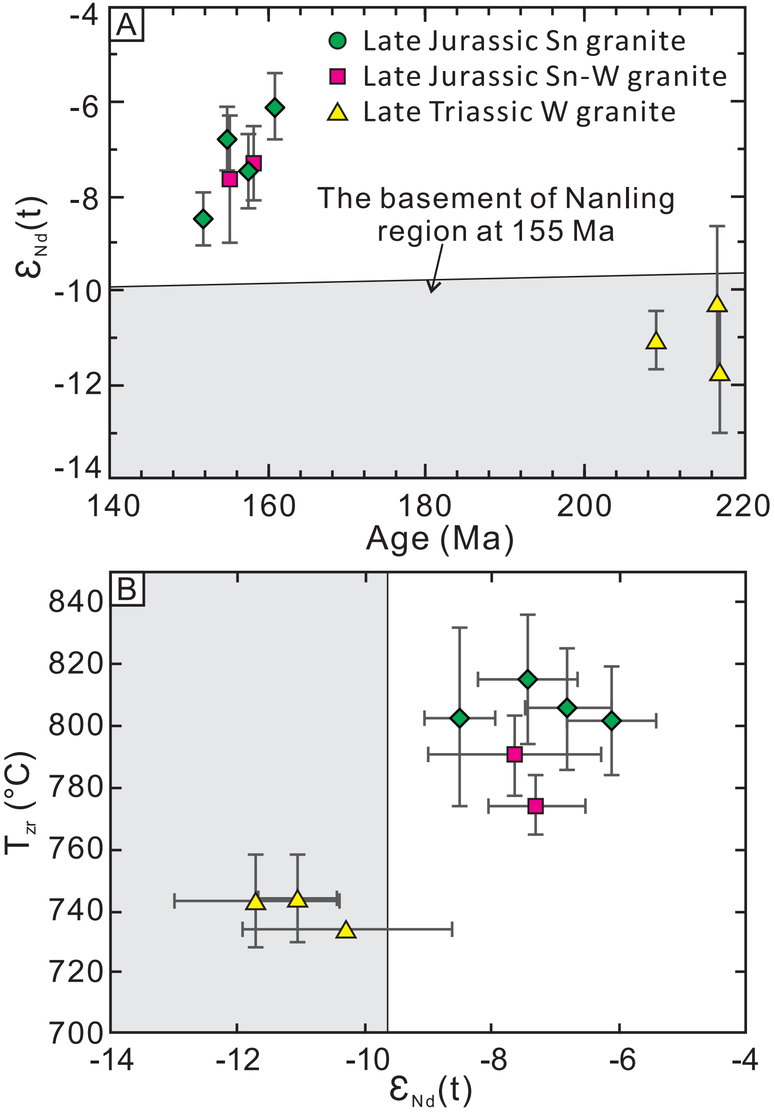
A
Late Jurassic Sn granite
Late Jurassic Sn-W granite
Late Triassic W granite
The basement of Nanling region at 155 Ma
$\varepsilon_{Nd}(t)$
-4
-6
-8
-10
-12
-14
140
160
180
200
220
Age (Ma)
B
T_{zr} (°C)
840
820
800
780
760
740
720
700
-14
-12
-10
-8
-6
-4
$\varepsilon_{Nd}(t)$

The zircon saturation thermometry was based on Watson and Harrison (1983), that defined experimentally the saturation behavior of zircon in crustal anatectic melts as a function of both temperature and composition:

$$\ln D_{Zr}^{zircon/melt} = \{-3.8 - [0.85*(M-1)]\} + 12900/T$$

Rearranging the equation to yield T a geothermometer for melt:

$$T = 12900/[\ln D_{Zr}^{zircon/melt} + 3.8 + 0.85*(M-1)]$$

Where $D_{Zr}^{zircon/melt}$ is the ratio of Zr concentration (ppm) in zircon (500,000 ppm) to that in the melt; T is the absolute temperature, and M is the cation ratio of (Na + K + 2*Ca)/(Al *Si). This thermometry applies to most intermediate to felsic magmas in the crust with magmatic temperature of 750 to 1000 °C (Watson and Harrison, 1983). Since the solubility of zircon is largely insensitive to pressure, the thermometry is not influenced by pressure. Boehnke et al. (2013) re-revisited this thermometry by improved experimental, analytical and fitting method and confirmed that the temperature and composition are the two dominant controls on zircon solubility in crustal melts with no observable effects due to pressure (up to 25 kbar) or variable water content. The refined model in Boehnke et al. (2013) predicts broadly similar temperatures for most melt compositions and temperatures as that of Watson and Harrison (1983), especially at low zircon concentrations and peraluminous melt which are the case of this manuscript.

The thermometry of Watson and Harrison (1983) has been widely used to constrain the melting temperature of granite. For example, Chappell et al. (1998, 2000, 2004) divided the granites in the Lachlan Fold Belt into low-temperature and high-temperature granites based on the melting temperature calculated by the zircon-saturation thermometer. Similarly, Miller et al. (2003) divided the investigated plutons into hot granites (mean 766 °C) and cold granites (mean 837 °C) based on zircon saturation thermometry.

Miller et al. (2003) further proposed that zircon saturation temperature provide minimum estimates of temperature if the magma was undersaturated in zirconium, but maxima if it was saturated. For the high-temperature granites formed from a magma in which crystals of zircon were not initially present because the melt was undersaturated in zircon. Along with the cooling downing of the magma, zircon start to crystallize when the magmatic temperature is lower than the zircon-saturation temperature. Therefore, for the granites without inherited zircon, the calculated zircon-saturation temperature might underestimate the true initial temperature of the magma (Chappell et al., 1998, 2000; Miller er al., 2003). For the granites full of inherited zircon, the magmas were zircon saturated at their source. The inherited zircon might artificially increase the Zr concentration of the magma, because part of their total Zr concentration is in crystals rather than melt, and thus the calculated zircon-saturation temperature should place an upper limit on initial magma temperature (Miller et al., 2003).

The W- and Sn-related granites studied in this study are felsic and peraluminous in composition and are derived from melting of crust. The zircon saturation temperature thermometry of Watson and Harrison (1983) should apply to the granites in this study. Since the low-temperature, W-related granite has abundant inherited zircon whereas the high-temperature Sn-related granite was inheritance-poor (this study and Zhang et al., 2015), the difference of the initial magma temperature for the W- and Sn-related granites should be even larger than estimated by zircon-saturation thermometry.

Reference

Boehnke, P., Watson, E.B., Trail, D., Harrison, T.M., and Schmitt, A.K., 2013, Zircon saturation re-revisited: Chemical Geology, v. 351, p. 324-334.

Chappell, B.W., Bryant, C.J., Wyborn, D., White, A.J.R., and Williams, I.S., 1998. High- and low-tempreature granites. Resource Geology, v. 48, p. 225-236.

Chappell, B.W., White, A.J.R., Williams, I.S., and Wyborn, D., 2004. Low- and high-tempreature granites. Trans. Royal. Soc. Edinburgh: Earth Sci. v.95, p. 125-140.

Chappell, B.W., White, A.J.R., Williams, I.S., Wyborn, D., and Wyborn, L.A.I., 2000. Lachlan Fold Belt granites revisited: High- and low-temperature granites and and their implications. Australian J. Earth Sciences, v. 47, p. 123-138.

Miller, C.F., McDowell, S.M., and Mapes, R.W., 2003, Hot and cold granites? Implications of zircon saturation temperatures and preservation of inheritance: Geology, v. 31, p. 529–532.

Watson, E.B., and Harrison, T. M., 1983, Zircon saturation revisited: temperature and composition effects in a variety of crustal magma types: Earth and Planetary Science Letters, v. 64, p. 295–304.

Zhang, R.Q., Lu, J.J., Wang, R.C., Yang, P., Zhu, J.C., Yao, Y., Gao, J.F., Li, C., Lei, Z.H., Zhang, W.L., and Guo, W.M., 2015, Constraints of in situ zircon and cassiterite U–Pb, molybdenite Re–Os and muscovite ^{40}Ar–^{39}Ar ages on multiple generations of granitic magmatism and related W–Sn mineralization in the Wangxianling area, Nanling Range, South China: Ore Geology Reviews, v. 65, p. 1021–1042.

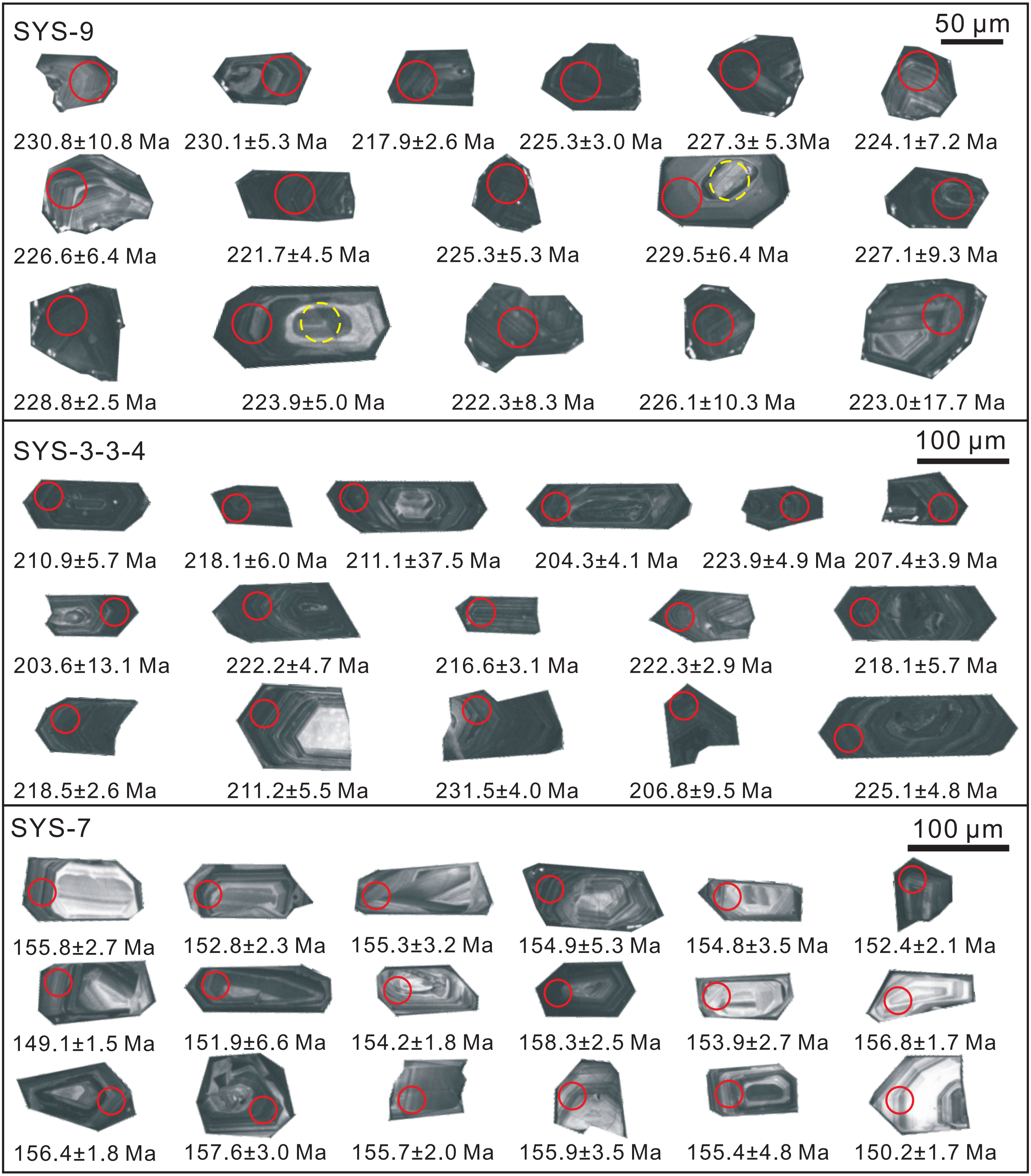
SYS-9
50 μm
230.8±10.8 Ma
230.1±5.3 Ma
217.9±2.6 Ma
225.3±3.0 Ma
227.3± 5.3Ma
224.1±7.2 Ma
226.6±6.4 Ma
221.7±4.5 Ma
225.3±5.3 Ma
229.5±6.4 Ma
227.1±9.3 Ma
228.8±2.5 Ma
223.9±5.0 Ma
222.3±8.3 Ma
226.1±10.3 Ma
223.0±17.7 Ma
SYS-3-3-4
100 μm
210.9±5.7 Ma
218.1±6.0 Ma
211.1±37.5 Ma
204.3±4.1 Ma
223.9±4.9 Ma
207.4±3.9 Ma
203.6±13.1 Ma
222.2±4.7 Ma
216.6±3.1 Ma
222.3±2.9 Ma
218.1±5.7 Ma
218.5±2.6 Ma
211.2±5.5 Ma
231.5±4.0 Ma
206.8±9.5 Ma
225.1±4.8 Ma
SYS-7
100 μm
155.8±2.7 Ma
152.8±2.3 Ma
155.3±3.2 Ma
154.9±5.3 Ma
154.8±3.5 Ma
152.4±2.1 Ma
149.1±1.5 Ma
151.9±6.6 Ma
154.2±1.8 Ma
158.3±2.5 Ma
153.9±2.7 Ma
156.8±1.7 Ma
156.4±1.8 Ma
157.6±3.0 Ma
155.7±2.0 Ma
155.9±3.5 Ma
155.4±4.8 Ma
150.2±1.7 Ma

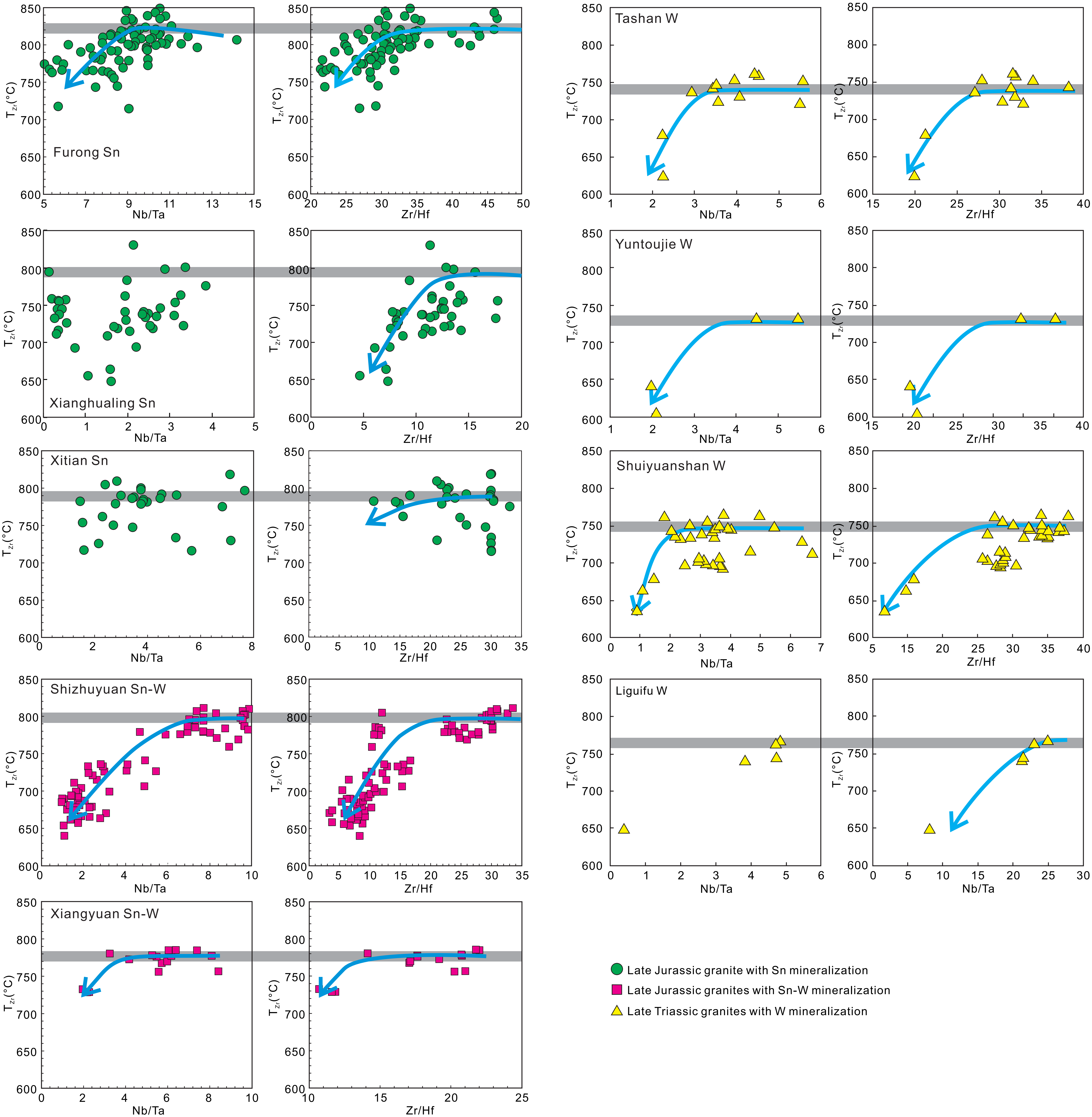
Furong Sn
Xianghualing Sn
Xitian Sn
Shizhuyuan Sn-W
Xiangyuan Sn-W
Tashan W
Yuntoujie W
Shuiyuanshan W
Liguifu W
T_Zr(°C)
Nb/Ta
Zr/Hf
Late Jurassic granite with Sn mineralization
Late Jurassic granites with Sn-W mineralization
Late Triassic granites with W mineralization

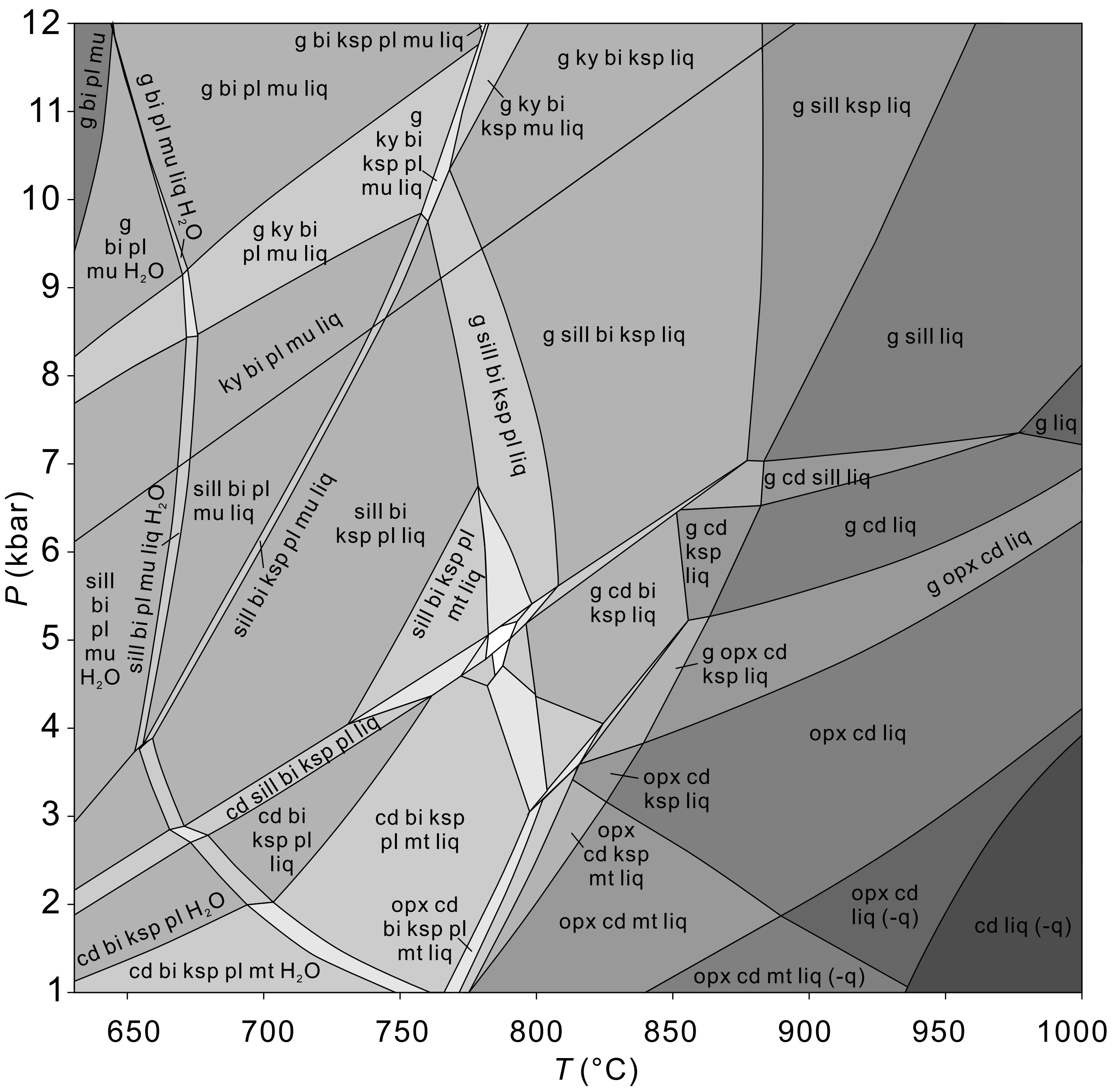

g bi pl mu
g bi pl mu liq H2O
g bi pl mu liq
g bi ksp pl mu liq
g ky bi ksp liq
g ky bi ksp mu liq
g ky bi ksp pl mu liq
g sill ksp liq
g bi pl mu H2O
g ky bi pl mu liq
g sill bi ksp liq
g sill liq
ky bi pl mu liq
g sill bi ksp pl liq
g liq
g cd sill liq
sill bi pl mu liq
sill bi ksp pl liq
sill bi pl mu liq H2O
sill bi ksp pl mu liq
g cd ksp liq
g cd liq
g opx cd liq
sill bi pl mu H2O
sill bi ksp pl mt liq
g cd bi ksp liq
g opx cd ksp liq
cd sill bi ksp pl liq
opx cd liq
opx cd ksp liq
cd bi ksp pl liq
cd bi ksp pl mt liq
opx cd ksp mt liq
cd bi ksp pl H2O
opx cd bi ksp pl mt liq
opx cd mt liq
opx cd liq (-q)
cd liq (-q)
cd bi ksp pl mt H2O
opx cd mt liq (-q)
P (kbar)
T (°C)
1
2
3
4
5
6
7
8
9
10
11
12
650
700
750
800
850
900
950
1000